

OPTICALLY PUMPED CARBON MONOXIDE CASCADE LASER

NICHOLAS W. SAWRUK

30 June 2005

Final Report

APPROVED FOR PUBLIC RELEASE; DISTRIBUTION IS UNLIMITED.



**AIR FORCE RESEARCH LABORATORY
Directed Energy Directorate
3550 Aberdeen Ave SE
AIR FORCE MATERIEL COMMAND
KIRTLAND AIR FORCE BASE, NM 87117-5776**

DTIC COPY

Using Government drawings, specifications, or other data included in this document for any purpose other than Government procurement does not in any way obligate the U.S. Government. The fact that the Government formulated or supplied the drawings, specifications, or other data, does not license the holder or any other person or corporation; or convey any rights or permission to manufacture, use, or sell any patented invention that may relate to them.

This report has been reviewed by the Public Affairs Office and is releasable to the National Technical Information Service (NTIS). At NTIS, it will be available to the general public, including foreign nationals.

If you change your address, wish to be removed from this mailing list, or your organization no longer employs the addressee, please notify AFRL/DELC, 3550 Aberdeen Avenue SE, Kirtland AFB, NM 87117-5776.

Do not return copies of this report unless contractual obligations or notice on a specific document requires its return.

This report has been approved for publication.

//signed//

DAVID A. HOSTUTLER DR-II
Program Manager

//signed//

KIP KENDRICK DR-III
Chief, Branch or Division

//signed//

BRUCE SIMPSON SES
Director, Directed Energy Directorate

REPORT DOCUMENTATION PAGE				Form Approved OMB No. 0704-0188	
<small>Public reporting burden for this collection of information is estimated to average 1 hour per response, including the time for reviewing instructions, searching existing data sources, gathering and maintaining the data needed, and completing and reviewing this collection of information. Send comments regarding this burden estimate or any other aspect of this collection of information, including suggestions for reducing this burden to Department of Defense, Washington Headquarters Services, Directorate for Information Operations and Reports (0704-0188), 1215 Jefferson Davis Highway, Suite 1204, Arlington, VA 22202-4302. Respondents should be aware that notwithstanding any other provision of law, no person shall be subject to any penalty for failing to comply with a collection of information if it does not display a currently valid OMB control number. PLEASE DO NOT RETURN YOUR FORM TO THE ABOVE ADDRESS.</small>					
1. REPORT DATE (DD-MM-YYYY) 30-06-05		2. REPORT TYPE Final Report		3. DATES COVERED (From - To) June 1 2001 - May 31	
4. TITLE AND SUBTITLE Optically Pumped Carbon Monoxide Cascade Laser				5a. CONTRACT NUMBER In House	
				5b. GRANT NUMBER	
				5c. PROGRAM ELEMENT NUMBER	
6. AUTHOR(S) Nicholas W. Sawruk				5d. PROJECT NUMBER 4866	
				5e. TASK NUMBER LB	
				5f. WORK UNIT NUMBER 07	
7. PERFORMING ORGANIZATION NAME(S) AND ADDRESS(ES) AFRL/DELC 3550 Aberdeen Avenue SE Kirtland AFB, NM 87117-5776				8. PERFORMING ORGANIZATION REPORT	
9. SPONSORING / MONITORING AGENCY NAME(S) AND ADDRESS(ES) Air Force Research 3550 Aberdeen Avenue SE Kirtland AFB, NM 87117-				10. SPONSOR/MONITOR'S ACRONYM(S)	
				11. SPONSOR/MONITOR'S REPORT NUMBER(S) AFRL-DE-PS-TR-2005-1093	
12. DISTRIBUTION / AVAILABILITY STATEMENT Approved for public release; distribution is unlimited.					
13. SUPPLEMENTARY NOTES Masters thesis of Capt. Nicholas Sawruk					
14. ABSTRACT The experimental and theoretical results of an optically pumped vibrational CO laser are explored. A tunable 1550-1580nm optical parametric oscillator laser was used as a pulsed pump source. The OPO pumped the R(6) through R(9) (3,0) overtone band of the CO, which induced lasing on the (3,2) and (2,1) bands around 4.7um. The laser output was spectrally separated to determine the spectral and temporal evolution of the CO lasing pulse. The influence of CO pressure, cell length, pump pulse intensity, and the resonator Q-Factor on the CO laser pulse temporal profile and spectral distribution were studied. A numerical model was developed, and the experimental results are compared to the model predictions.					
15. SUBJECT TERMS CO cascade laser					
16. SECURITY CLASSIFICATION OF:			17. LIMITATION OF ABSTRACT unlimited	18. NUMBER 114	19a. NAME OF RESPONSIBLE PERSON
a. REPORT unclassified	b. ABSTRACT unclassified	c. THIS PAGE unclassified			19b. TELEPHONE NUMBER (include area code) 505-853-2680

Table of Contents

Table of Contents	iii
List of Figures	vii
List of Tables	xi
ACKNOWLEDEMENTS	xii
SUMMARY	1
CHAPTER ONE: INTRODUCTION	2
1.1 The Optically Pumped Carbon Monoxide Laser	2
1.2 Previous Studies	3
1.3 Thesis Layout	4
CHAPTER TWO: THEORY OF THE CO CASCADE LASER	5
2.1 Rotational / Vibrational Energy Levels	5
Spectroscopy Notation	9
Anharmonic Potential and Other Higher Order Terms	10
2.2 Selection Rules	13
2.3 Thermal Population	18
2.4 Kinetic Processes	20
Vibrational-Vibrational (V-V) Transitions	21
Vibrational-Translational (V-T) Transitions	21
Rotational-Relaxation (R-R)	22
Absorption with Instantaneous R-R and Slow R-R Conditions	22

<u>Determining R-R Rate Constants</u>	24
<u>2.5 Radiative Processes</u>	Error! Bookmark not defined.
<u>2.6 Line Shape, Gain, and Absorption</u>	27
<u>Line Shape</u>	27
<u>Pressure Broadening</u>	28
<u>Gain</u>	32
<u>Absorption: Beer-Lambert</u>	35
<u>Amplified Spontaneous Emission (ASE)</u>	35
<u>Laser Gain with Instantaneous R-R and Slow R-R</u>	36
<u>2.7 The Resonator and Cavity Modes</u>	37
<u>Axial Modes of a Resonator</u>	38
<u>Transverse Modes of a Resonator</u>	39
<u>Mode Spacing</u>	39
<u>2.8 Mode Locking</u>	41
<u>CHAPTER THREE: EXPERIMENTAL AND PROCEDURES</u>	46
<u>3.1 OPO Specifics</u>	47
<u>Nd:YAG</u>	49
<u>CW Diode Seed Laser</u>	50
<u>OPO Wavelength Tuning</u>	51
<u>OPO Operation and Alignment Procedure</u>	53
<u>OPO Alignment</u>	54

<u>The OPO Pulse</u>	56
<u>OPO Operating Procedures</u>	59
<u>3.2 CO Lasing Cell</u>	60
<u>3.3 Photodetectors</u>	61
<u>3.4 Monochromator Operation</u>	63
<u>3.5 Data Acquisition: Oscilloscope</u>	64
<u>CHAPTER FOUR: RESULTS AND DISCUSSION</u>	67
<u>4.1 Lineshape Analysis and Pressure Broadening Coefficients</u>	67
<u>4.2 CO Lasing Results Short Gain</u>	68
<u>4.3 CO Lasing Results Long Gain</u>	77
<u>4.4 Discussion</u>	84
<u>REFERENCES</u>	93
<u>APPENDIX A: DATA PLOTS</u>	97
<u>APPENDIX B: LINEWIDTH EXPERIMENTS</u>	104
<u>APPENDIX C: Numerical Model Description</u>	106

List of Figures

CHAPTER ONE: INTRODUCTION

Figure 1.1. Atmospheric transmission spectrum.....	3
--	---

CHAPTER TWO: THEORY OF CO CASCAD LASER

Figure 2.1. Distances used in the hydrogen molecule Hamiltonian,	6
Figure 2.2. Potential well, harmonic & anharmonic,	9
Figure 2.3. Harmonic and Anharmonic potential wells. . .	11
Figure 2.4. Vibrational and rotational distribution of CO at room temperature,	20
Figure 2.5. Lorentzian, Gaussian, and Voigt profiles,	32
Figure 2.6. Transverse Mode Patterns,	39
Figure 2.7. Mode spacing and allowed laser frequencies,.....	40
Figure 2.8. Plot of 4 modes oscillating with random phases,	42
Figure 2.9. Intensity traces of mode locked pulse train for 4 and 8 modes. .	44
Figure 2.10. FFT of a mode locked pulse trains containing 8 and 4 modes respectively.	
.....	45

CHAPTER THREE: EXPERIMENTAL AND PROCEDURES

Figure 3.1. The top level experimental setup,	46
Figure 3.2. The OPO's setup,.....	47
Figure 3.3. Seeded versus unseeded Nd:YAG operation,	50
Figure 3.4. Blow up of OPO resonator,	54

Figure 3.5. Aligned OPO bleed through..	56
Figure 3.6. Typical spatial profile of the OPO pump pulse.	57
Figure 3.7. Short resonator with a double passed focused pump pulse..	58
Figure 3.8. OPO temporal profile and bandwidth..	59
Figure 3.9. Carbon Monoxide laser cell schematic.	52
Figure 3.10 Screen shot of the data acquisition program.....	56
Figure 3.11. Experimental layout	65
Figure 3.12. Averaging effects..	66

CHAPTER FOUR: RESULTS AND DISCUSSIONS

Figure 4.1. The lineshapes	68
Figure 4.2. Energy level diagram of pumped transition.	69
Figure 4.3. Fundamental resonator mode and pump pulse.	70
Figure 4.4. Multi-transverse mode lasing.	71
Figure 4.5. FFT of the multi-mode CO laser pulse.	71
Figure 4. 6. Multimode and single mode operation.	72
Figure 4.7. Pump absorption versus CO pressure through a 1.82m static CO cell.	73
Figure 4.8. A typical plot of the spectrally resolved CO laser pulse.	76
Figure 4.9. Typical plot of the spectrally resolved CO pulse.	77
Figure 4.10. Mode-Locked pulse train.	78
Figure 4.11. The FFT of the mode-locked $v(3,2)P(8)$ lasing line.	79
Figure 4.12. Long cavity resonator fundamental mode volume	81

Figure 4.13. CO laser pulse	82
Figure 4.14. Spectrally resolved lasing output	83
Figure 4.15. Spectrally resolve lasing output	84
Figure 4.16. Experimental output energy versus output coupler transmission	85
Figure 4.17. Power output versus pressure with a 40% reflective output coupler	85

CHAPTER FIVE: FUTURE STUDY

Figure 5.1. CO laser output with a 25kW CW pump source	89
Figure 5.2. Boltzmann rotational distribution for the ground state of CO	90
Figure 5.3. Efficiency versus pump power	91
Figure 5.4. Absorption versus pump power	92
Figure 5.5. Absorption versus path length	92
Figure 5.6. The Isat curve for 30 Torr of CO at 298K and 100K	93

APPENDIX A: Data Plots

Figure A.1. 95% reflective output coupler and 100 - 10 Torr of CO	98
Figure A.2. 70% reflective output coupler and 100 - 5 Torr of CO	99
Figure A.3. 60% reflective output coupler and 100 - 5 Torr of CO	100
Figure A.4. 40% reflective output coupler and 100 - 5 Torr of CO	101
Figure A.5. % reflective output coupler and 100 - 5 Torr of CO	102
Figure A.6. ASE emission plots for various pressures	103

APPENDIX C: Numerical Model Description

Figure C.1. The negligible effects of VV and VT kinetics.	110
Figure C.2. Model output of an v(0,3)R(6) pump case.	111

List of Tables

CHAPTER TWO: THEORY OF CO CASCADE LASER

Table 2.1. Spectroscopic constants	10
Table 2.2. The energies, wavelengths, and A coefficients for , v (3,2).	14
Table 2.3. The energies, wavelengths, and A coefficients for , v (2,1).	15
Table 2.4. CO self-pressure broadening coefficients for [22].	29

CHAPTER THREE: EXPERIMENTAL AND PROCEDURES

Table 3.1. The v(0,3) pump transition energies	52
--	----

CHAPTER FOUR: RESULTS AND DISCUSSIONS

Table 4. 1. Experimental specifications for all following results.	80
--	----

CHAPTER FIVE: FUTURE STUDY

Table 5.1. Model input conditions for CW pumping runs.....	79
--	----

ACKNOWLEDEMENTS

This work was funded by the United States Air Force and was performed at the Air Force Research Laboratory's High Power Gas and Chemical Laser Branch (AFRL/DELC) at Kirtland Air Force Base, Albuquerque, New Mexico. I am very grateful for the assistance of the branch members and contractors.

In particular I would like to thank the Dr. Gordon Hager for the many enlightened conversations, and his love for science. Dr. David Hostutler provided me with daily advice and guidance, and I would not have been successful with Dr. Hostutler's support. I would also like to acknowledge my thesis advisor, Dr. John K. McIver, who provided invaluable incite into my research.

I would also like to thank the mathematics department at the United States Air Force Academy for sponsoring me to finish my graduate degree.

SUMMARY

The experimental and theoretical results of an optically pumped vibrational CO laser are explored. A tunable 1550-1580nm optical parametric oscillator laser was used as a pulsed pump source. The OPO pumped the R(6) through R(9) (3,0) overtone band of the CO, which induced lasing on the (3,2) and (2,1) bands around 4.7 μ m. The laser output was spectrally separated to determine the spectral and temporal evolution of the CO lasing pulse. The influence of CO pressure, cell length, pump pulse intensity, and the resonator Q-Factor on the CO laser pulse temporal profile and spectral distribution were studied. A numerical model was developed, and the experimental results are compared to the model predictions.

CHAPTER ONE: INTRODUCTION

1.1 The Optically Pumped Carbon Monoxide Laser

This dissertation describes the most extensive investigation into a 2nd overtone optically pumped Carbon Monoxide, CO, laser to date. The 2nd overtone CO laser consists of a pulsed pump source operating at approximately 1.5 μm used to excite various rotational transitions on the 2nd overtone band of CO. The CO lases twice on two successive inversions, first from the (3,2) band and then from the (2,1) band both around 4.7 μm . This thesis is intended to adequately describe the radiative and kinetic processes that affect the optically pumped CO laser and to shed light on future improvements to the 4 micron CO cascade laser.

Carbon monoxide has been developed as a high power electric discharge laser; it was first developed in 1964 at Bell Laboratories [1]. The electric-discharge CO lasers operate on a many high lying fundamental bands, and exhibit broad band output around 5-6 μm [2]-[3]. However, the atmospheric absorption window is closed in the output region of the electric discharge CO laser, see Figure 1.1. Optically pumping CO provides a mean to excite a specific rovibrational level, and lase on a single fundamental band at a wavelength around 4.7 μm , which falls within the atmospheric window. Another useful application of optically pumping the 2nd overtone of CO is the convenient wavelength required, 1560-1576 μm . This wavelength happens to coincide with Erbium fiber laser wavelengths, which have been developed for the telecommunication industry. Optically pumping CO shows potential as an efficient

means to beam combine and frequency convert the output of a high power fiber laser bundle to a single $4.76\mu\text{m}$ beam with good beam quality.

Various aspects of the CO lasing process were studied experimentally and theoretically and will be presented in this thesis. The influence of CO pressure, cell length, pump pulse intensity, and the resonator Q-Factor on the CO laser pulse temporal profile and spectral distribution were studied. A numerical model was developed, and the experimental results are compared to the model predictions. At longer gain and resonator lengths (2m) the CO laser ran in mode locked operation.

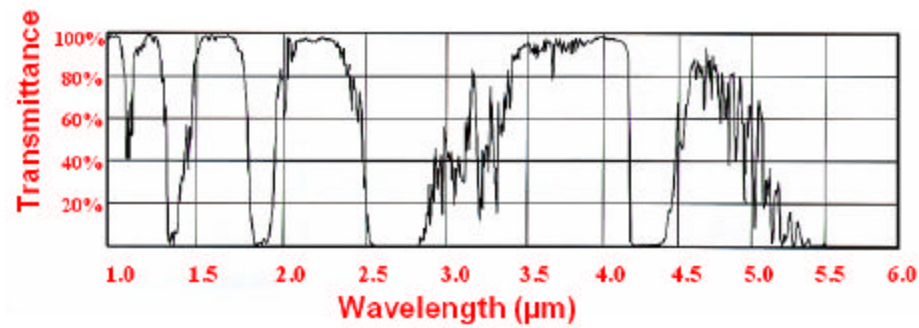


Figure 1.1. Atmospheric transmission spectrum. Notice the high transmission around $4.6\text{--}4.8\mu\text{m}$.

Optically pumping a molecular gas shows potential in becoming a viable means to produce a high power $4.6\mu\text{m}$ laser system. The wavelength region around $4.6\text{--}4.8\mu\text{m}$ is of great interest due to the atmospheric window in that region, Figure 1.1.

1.2 Previous Studies

Carbon monoxide has been used as an optically pumped lasing medium in the past. The experiments conducted at AFRL demonstrated CO's ability to be optically pumped at 2.36 μm and lase from the 1st overtone band [4]-[5]. McCord demonstrated multi-line lasing in (2,1) band of CO with a reported efficiency of 25% in 1999 [4]. Further work by McCord showed single line lasing, with a reported efficiency of 13% from the (2,1) band by introducing a grating into the resonator [5].

Various other molecular gasses such as HBr and HCl, were optically pumped to higher vibrational overtones [6]-[8]. Both gasses successfully produced cascade laser outputs around 4 μm . The above mentioned research was referenced heavily for experimental approaches and considerations.

1.3 Thesis Layout

Chapter 2 reviews the various theoretical concepts required to adequately understand and model this CO laser. A brief discussion of the following topics are included to refresh the reader; diatomic vibration rotational energy, kinetic processes, radiative processes, transverse and axial resonator modes, and mode locking. The discussions are not intended to be complete in their theoretical derivation, but rather act as a basic guide to the physics used in the data analysis.

Chapter 3 outlines the experimental setup and procedures used in the laser experiments in great detail. All the instruments used in the data collection will be adequately documented. The operating and aligning procedures for the optical parametric oscillator are included as a reference for future research.

The results and conclusions of both the theoretical and experimental data will be presented in Chapter 4. Chapter 5 contains a brief discussion of a future research effort in continuous wave pumping of CO.

CHAPTER TWO: THEORY OF THE CO CASCADE LASER

2.1 Rotational / Vibrational Energy Levels

The energy levels of a quantum mechanical system are defined by the solution to the Schrödinger wave equation.

$$\hat{H} \Psi_M = E_M \Psi_M \quad (2.1)$$

Where \hat{H} is the Hamiltonian operator, Ψ_M represents a molecule's wave function and E_M is the total energy of the system including electronic, vibrational, rotational, and translational energy [9]. The Hamiltonian of a hydrogen molecule is:

$$\begin{aligned} \hat{H} = & \frac{-\hbar^2}{2M} (\nabla_A^2 + \nabla_B^2) - \frac{\hbar^2}{2m_e} (\nabla_1^2 + \nabla_2^2) - \frac{e^2}{4\pi\epsilon_0} \left[\frac{1}{r_{1A}} + \frac{1}{r_{1B}} + \frac{1}{r_{2A}} + \frac{1}{r_{2B}} \right] \\ & + \frac{e^2}{4\pi\epsilon_0} \left[\frac{1}{r_{12}} + \frac{1}{R} \right] \end{aligned} \quad (2.2)$$

where M is the mass of the hydrogen nucleus, m_e is the mass of an electron, subscripts 1 and 2 refer to the two electrons, subscripts A and B refer to the two hydrogen nuclei, ∇ is the Laplacian operator, and the distances for $r_{i,j}$ are found in Figure 2.1.

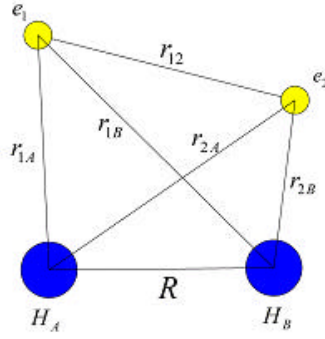


Figure 2.1. Distances used in the hydrogen molecule Hamiltonian.

The first four terms represent the kinetic energy of both nuclei and electrons respectively. The next four terms represent the potential energy from electron-nuclei interactions. The second to last term is the repulsion potential energy between the two electrons, and the last term is the repulsion potential energy between the nuclei.

The hydrogen molecule is used as an example for its simplicity, and the more general Hamiltonian for any diatomic molecule can be easily developed using the hydrogen molecule as an example.

$$\hat{H} = \frac{-\hbar^2}{2M_A} \nabla_A^2 - \frac{\hbar^2}{2M_B} \nabla_B^2 - \frac{\hbar^2}{2m_e} \sum_i \nabla_i^2 - \sum_i \frac{Z_A e^2}{r_{Ai}} - \sum_i \frac{Z_B e^2}{r_{Bi}} + \sum_{i,j} \frac{e^2}{r_{i,j}} + \frac{Z_A Z_B}{R} \quad (2.3)$$

The summations in equation 2.3 allow for an indefinite amount of electrons in the diatomic molecule, and Z is the nucleus charge.

In order to solve the differential equation, a few substitutions and assumptions must be made. First, the wave equation is separated into two parts, nuclear and electronic:

$$\Psi_M(r, R) = \Psi_N(R) \Psi_{el}(r, R) \quad (2.4)$$

where $\Psi_N(R)$ is the nuclear portion, and $\Psi_{el}(r, R)$ is the electronic portion.

Substituting equation 2.4 into 2.1, applying the common vector calculus identity,

$$\nabla^2[fg] = f\nabla^2g + 2\nabla f \nabla g + g\nabla^2f \quad (2.5)$$

and using the Born Oppenheimer approximation drastically simplifies the Schrödinger equation. The Born Oppenheimer approximation simply states that electrons respond instantaneously with respect to nuclear motion since the mass of an electron is much less than that of a nucleus [10]. Also, to first order the electron forces have no effect on the nuclear energy. This approximation forces all differential terms involving both the electron and nuclear energies to have a value of zero, and can be written as:

$$\begin{aligned} \nabla_{A,B} \Psi_{el} &= 0 & \nabla_i \Psi_N &= 0 \\ \nabla_{A,B}^2 \Psi_{el} &= 0 & \nabla_i^2 \Psi_N &= 0 \end{aligned} \quad (2.6)$$

The Schrödinger equation can now be written as:

$$\begin{aligned} E_M \Psi_N \Psi_{el} &= \frac{-\eta^2}{2M_A} [\Psi_{el} \nabla_A^2 \Psi_N] - \frac{\eta^2}{2M_B} [\Psi_{el} \nabla_B^2 \Psi_N] - \frac{\eta^2}{2m_e} \sum_i [\Psi_N \nabla_i^2 \Psi_{el}] \\ &+ [V_{NN} + V_{ee} + V_{Ne}] \Psi_N \Psi_{el} \end{aligned} \quad (2.7)$$

The equation is now separable into nuclear and electronic parts.

$$\begin{aligned} \frac{-\eta^2}{2m_e} \sum_i \nabla_i^2 \Psi_{el} + (V_{NN} + V_{ee} + V_{Ne}) &= C \Psi_{el} \\ \frac{-\eta^2}{2} \left[\frac{1}{M_A} \nabla_A^2 \Psi_N + \frac{1}{M_B} \nabla_B^2 \Psi_N \right] &= -C \Psi_N + E_M \Psi_N \end{aligned} \quad (2.8)$$

The separation constant, C, represents the total electronic energy in a diatomic molecule, and is a function of the internuclear separation, U(r). The total nuclear

energy of the molecule can be solved by further separating the wave function into angular and radial parts: $\Psi(R, \mathbf{q}, \mathbf{f}) = R(r)Y(\mathbf{q}, \mathbf{f})$. The solutions to the angular part of the nuclear Schrödinger equation are the rigid rotor wave functions, which are called spherical harmonics [11]. The rotational energy levels of a diatomic molecule using the rigid rotor model are given by:

$$E_J = \frac{\hbar^2}{2I} J(J+1) \quad J = 0, 1, 2, \dots \quad (2.9)$$

where I is the molecule's moment of inertia using the center of mass approximation. Each energy level has a degeneracy of $g_J = 2J + 1$, and only $\Delta J = \pm 1$ transitions are allowed. The selection rules for rotational transitions will be explored at a later time.

The radial portion, $R(r)$, of the nuclear Schrödinger equation results in vibrational energy levels, and the form of $U(r)$ must be known. Typically, $U(r)$ can be represented by a parabolic oscillator for a first order approximation. The Taylor series expansion around r_0 , where r_0 is the equilibrium bond length, is:

$$U(r) = U(r_0) + U'(r_0)(r - r_0) + \frac{1}{2!} U''(r_0)(r - r_0)^2 + \frac{1}{3!} U'''(r_0)(r - r_0)^3 + \dots \quad (2.10)$$

The potential energy is zero, $U(r_0) = 0$ at the equilibrium bond length. By definition the first derivative at r_0 is also equal to zero, since the potential energy curve is at a minimum at r_0 . Using the first order approximation for the potential energy function, one can easily see it is a parabolic harmonic oscillator function, see Figure 2.2.

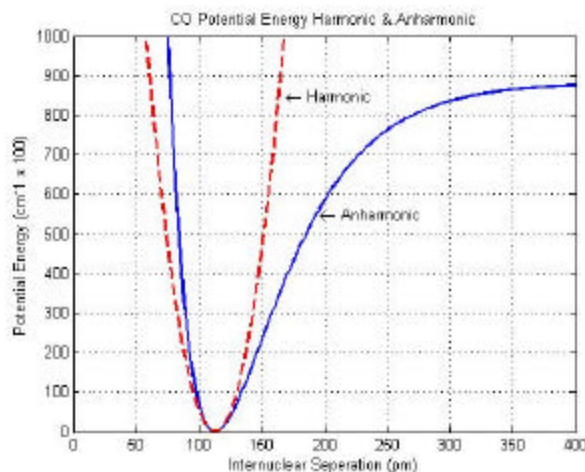


Figure 2.2. Potential well, harmonic & anharmonic.

The solution to the radial portion of the nuclear Schrödinger equation results in Hermite polynomials and discrete vibrational energy levels.

$$E_v = w_e (v + \frac{1}{2}) \quad v = 0, 1, 2, \dots \quad (2.11)$$

w_e is the zero point energy, and vibrational transitions are limited to $\Delta v = \pm 1$ by selections rules.

Spectroscopy Notation

A brief discussion of the spectroscopy notation used through out this thesis is in order here. A list of CO spectroscopic constants can be found in Table 2.1 published by Dunham [12]. The importance of each term will be developed in the following sections. A P-branch transition is defined as $\Delta J = J_{Upper} - J_{Lower} = -1$, and

an R-branch transition is $\Delta J = 1$. The rotational transitions will be written as $P(J_{Lower})$ and $R(J_{Lower})$. The notation used for vibrational transitions is $v(0,3)$ which means the transition from the ground vibrational state to the 3rd vibrational level or the 2nd overtone, and $v(3,2)$ describes the transition from the 3rd vibrational level to the 2nd vibrational level. For example consider the $v(0,3)R(6)$ transition, this rovibrational transition is from the $J=6$ rotational level within the ground state vibrational manifold to the 3rd vibrational manifold at the $J=7$ rotational level.

Anharmonic Potential and Other Higher Order Terms

The above results for a diatomic molecule using the rigid rotor and harmonic oscillator models provides a good first order approximation, but a more precise model is

Table 2.1. Spectroscopic constants

Constant	Value (cm ⁻¹)
w_e	2169.8124
$w_e c_e$	13.2879
\tilde{B}_e	1.9312
\tilde{D}_e	6.12E-06
a_e	0.0175

required to adequately model the second overtone pumping of CO. Figure 2.3 shows the harmonic oscillator is good approximation for small rovibrational transitions, $\Delta v = \pm 1$. However, for higher overtone transitions, the deviation between the harmonic and anharmonic potential grows as seen in Figure 2.3.

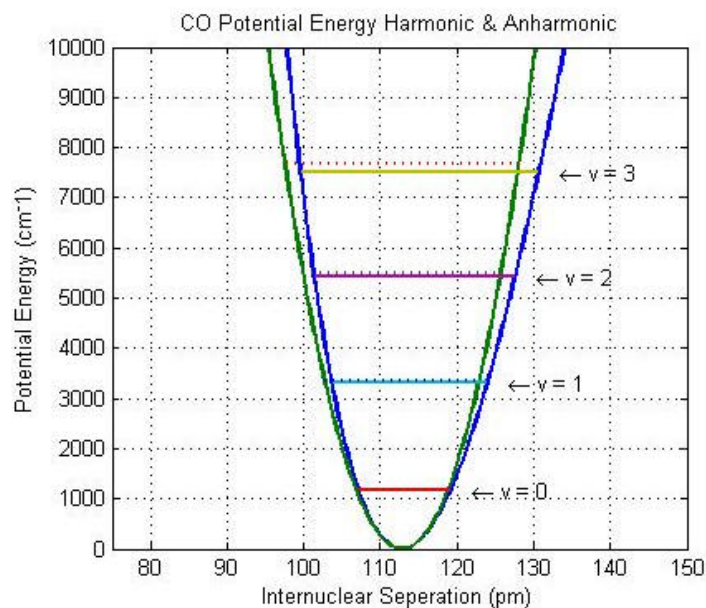


Figure 2.3. Harmonic and Anharmonic potential wells. For $v = 0, 1$ the harmonic potential is a close approximation, but for $v = 2+$ it begins to deviate.

The model can be drastically improved by including the anharmonic oscillator terms, rotational-vibrational interactions, and rotational effects. The harmonic oscillator model can be improved by including higher order terms in the Taylor series expansion of $U(r)$ as shown in equation 2.10.

Rotational transitions are super imposed upon vibrational transitions. Therefore, it is convenient to write the equation for a rovibrational transition [13].

$$E_{v,J} = E_v + E_J = \omega_e(v + \frac{1}{2}) + \tilde{B}J(J+1) \quad (2.12)$$

$$\tilde{B} = \frac{h}{8\pi^2 c I} \quad [cm^{-1}] \quad (2.13)$$

Molecules are not 100% rigid. As the rotational energy grows (higher J levels), the centrifugal force causes the bonds to stretch [14]. The stretching is a small effect and can be corrected for using perturbation theory resulting in a centrifugal distortion term, \tilde{D} .

$$E_J = \tilde{B}J(J+1) - \tilde{D}J^2(J+1)^2 \quad (2.14)$$

A similar effect on bond length occurs with vibrational transitions, causing the rotational energy to have a vibrational dependency. As the vibrational energy increases, the inter-nuclear bond length also increases vibration-rotation interaction [14]. The vibrational dependent rotational energy is:

$$E_J = \tilde{B}_v J(J+1) - \tilde{D}J^2(J+1)^2 \quad (2.15)$$

$$\tilde{B}_v = \tilde{B}_e - \alpha_e(v + \frac{1}{2}) \quad (2.16)$$

The harmonic oscillator model must also be improved by including higher order terms. The higher order terms are termed anharmonicity constants. The resulting potential function can be seen in Figure 2.2. The equation for the vibrational energy including the higher order terms is:

$$E_v = \omega_e(v + \frac{1}{2}) - \omega_e x_e(v + \frac{1}{2})^2 + \omega_e y_e(v + \frac{1}{2})^3 \quad (2.17)$$

where $\tilde{\alpha}_e \ll 1$. Now the total rovibronic energy of a diatomic molecule can be written as:

$$E_{v,J} = \tilde{\nu}_{el} + \omega_e(v + \frac{1}{2}) - \omega_e x_e(v + \frac{1}{2})^2 + \omega_e y_e(v + \frac{1}{2})^3 + \tilde{B}_v J(J+1) - \tilde{D}J^2(J+1)^2 \quad (2.18)$$

The energy associated with vibrational transitions is approximately 100 to 1000 times that of rotational transitions. The energies and Einstein A coefficients associated with common transitions in this research project can be found in Tables 2.2-2.3.

2.2 Selection Rules

The rovibrational selection rules ($\Delta v = \pm 1, \Delta J = \pm 1$) stated in the previous section are derived from the time-dependent version of the Schrödinger's equation [15]. The time dependent Schrödinger's equations is:

$$\hat{H}\Psi = i\hbar \frac{\partial \Psi(r, t)}{\partial t} \quad (2.19)$$

$$\Psi(r, t) = \Psi_n(r) e^{-iE_n t / \hbar} \quad (2.20)$$

where equation 2.20 is the time dependent wave equation, and $\Psi_n(r)$ refers to the stationary states, unchanging with time. Now consider a non-stationary state system where an electric field interacts with a molecule. The electric field of interest will be written as:

$$\bar{E} = \bar{E} \cos(2\pi \nu t) \quad (2.21)$$

Table 2.2. The energies, wavelengths, and A coefficients for v (3,2).

Jlower	v = 3 to v = 2					
	R-Branch			P-Branch		
	cm ⁻¹	nm	A (Hz)	cm ⁻¹	nm	A (Hz)
0	2094.1099	4775.2986	33.2477	-	-	-
1	2097.8146	4766.8655	40.1147	2086.5951	4792.4966	98.6617
2	2101.4840	4758.5420	43.2121	2082.7854	4801.2628	65.4080
3	2105.1180	4750.3275	45.0525	2078.9410	4810.1414	58.5366
4	2108.7164	4742.2213	46.3210	2075.0620	4819.1332	55.4334
5	2112.2791	4734.2229	47.2810	2071.1486	4828.2388	53.5859
6	2115.8059	4726.3315	48.0555	2067.2009	4837.4592	52.3088
7	2119.2966	4718.5467	48.7097	2063.2191	4846.7949	51.3386
8	2122.7512	4710.8677	49.2811	2059.2034	4856.2468	50.5523
9	2126.1694	4703.2941	49.7930	2055.1538	4865.8158	49.8848
10	2129.5512	4695.8252	50.2607	2051.0706	4875.5026	49.2986
11	2132.8963	4688.4605	50.6944	2046.9538	4885.3080	48.7702
12	2136.2047	4681.1994	51.1014	2042.8037	4895.2329	48.2844
13	2139.4761	4674.0415	51.4870	2038.6203	4905.2782	47.8310
14	2142.7105	4666.9861	51.8549	2034.4039	4915.4448	47.4027
15	2145.9076	4660.0328	52.2082	2030.1545	4925.7334	46.9943
16	2149.0674	4653.1811	52.5490	2025.8724	4936.1451	46.6018
17	2152.1897	4646.4305	52.8792	2021.5576	4946.6808	46.2224
18	2155.2744	4639.7805	53.2001	2017.2103	4957.3414	45.8537
19	2158.3212	4633.2307	53.5128	2012.8306	4968.1279	45.4941
20	2161.3301	4626.7806	53.8182	2008.4188	4979.0412	45.1420
21	2164.3009	4620.4297	54.1171	2003.9749	4990.0824	44.7965
22	2167.2334	4614.1777	54.4100	1999.4991	5001.2525	44.4565
23	2170.1275	4608.0241	54.6974	1994.9916	5012.5524	44.1214
24	2172.9831	4601.9685	54.9798	1990.4525	5023.9833	43.7905
25	2175.8000	4596.0106	55.2574	1985.8819	5035.5462	43.4633
26	2178.5781	4590.1499	55.5306	1981.2800	5047.2423	43.1394
27	2181.3172	4584.3860	55.7997	1976.6469	5059.0725	42.8185
28	2184.0171	4578.7187	56.0647	1971.9828	5071.0381	42.5002
29	2186.6778	4573.1474	56.3259	1967.2879	5083.1402	42.1843

where ω is the frequency. The Hamiltonian operator for the interaction between an electric field and a molecule is written as:

$$\hat{H}^{(1)} = -\mathbf{m} \cdot \mathbf{E} = -\mathbf{m} \cdot E_0 \cos(2\pi \nu t) \quad (2.22)$$

where the superscript ⁽¹⁾ is used to denote the perturbation portion of the Schrödinger's equation listed below.

$$\hat{H} = \hat{H}^{(0)} + \hat{H}^{(1)} \quad (2.23)$$

Table 2.3. The energies, wavelengths, and A coefficients for v (2,1).

Jlower	v = 2 to v = 1					
	R-Branch			P-Branch		
	cm ⁻¹	nm	A (Hz)	cm ⁻¹	nm	A (Hz)
0	2120.5647	4715.7251	23.0686	-	-	-
1	2124.3044	4707.4233	27.8341	2112.9799	4732.6526	68.4542
2	2128.0088	4699.2286	29.9844	2109.1352	4741.2798	45.3804
3	2131.6778	4691.1404	31.2625	2105.2558	4750.0167	40.6117
4	2135.3112	4683.1581	32.1440	2101.3418	4758.8641	38.4576
5	2138.9089	4675.2810	32.8115	2097.3934	4767.8228	37.1748
6	2142.4707	4667.5085	33.3503	2093.4107	4776.8935	36.2878
7	2145.9964	4659.8401	33.8057	2089.3939	4786.0769	35.6138
8	2149.4860	4652.2751	34.2037	2085.3432	4795.3737	35.0675
9	2152.9392	4644.8130	34.5606	2081.2586	4804.7849	34.6037
10	2156.3560	4637.4533	34.8867	2077.1404	4814.3111	34.1962
11	2159.7361	4630.1953	35.1894	2072.9886	4823.9531	33.8289
12	2163.0795	4623.0387	35.4736	2068.8035	4833.7118	33.4913
13	2166.3859	4615.9828	35.7430	2064.5851	4843.5881	33.1761
14	2169.6553	4609.0271	36.0002	2060.3337	4853.5827	32.8784
15	2172.8874	4602.1712	36.2473	2056.0493	4863.6965	32.5946
16	2176.0822	4595.4146	36.4858	2051.7322	4873.9305	32.3218
17	2179.2395	4588.7567	36.7170	2047.3824	4884.2855	32.0582
18	2182.3592	4582.1972	36.9418	2043.0001	4894.7624	31.8020
19	2185.4410	4575.7355	37.1610	2038.5854	4905.3622	31.5522
20	2188.4849	4569.3713	37.3752	2034.1386	4916.0859	31.3076
21	2191.4907	4563.1041	37.5849	2029.6597	4926.9343	31.0676
22	2194.4582	4556.9335	37.7906	2025.1489	4937.9084	30.8316
23	2197.3873	4550.8590	37.9925	2020.6064	4949.0093	30.5989
24	2200.2779	4544.8804	38.1910	2016.0323	4960.2381	30.3692
25	2203.1298	4538.9971	38.3862	2011.4267	4971.5956	30.1421
26	2205.9429	4533.2089	38.5785	2006.7898	4983.0830	29.9173
27	2208.7170	4527.5153	38.7679	2002.1217	4994.7014	29.6946
28	2211.4519	4521.9161	38.9546	1997.4226	5006.4518	29.4738
29	2214.1476	4516.4107	39.1387	1992.6927	5018.3353	29.2547

The $\hat{H}^{(1)}$ will be treated as a small perturbation to the standard time dependent Hamiltonian, equation 2.19. The selection rules will be derived from a two-state system in which the wave equation is written as a linear combination of two wave functions,

one for each state. Each state is multiplied by a probability function that depends on time. At time zero, the system is only in state 1, $a_1(t=0)=1$, $a_2(t=0)=0$.

$$\Psi(t) = a_1(t)\Psi_1(t) + a_2(t)\Psi_2(t) \quad (2.24)$$

After substituting this back into equation 2.23 and after some simplification and manipulation the following results are found:

$$\frac{da_2}{dt} \propto C \cdot \int \Psi_2^* \mathbf{m}_z \Psi_1 dt \quad (2.25)$$

The time rate of change of a_2 represents the rate at which the system is changing from state 1 to state 2. C is simply a constant term containing the energies of the two states and the energy of the incident electric field and does not determine the probability of the transition. The integral in equation 2.25 is the key component in deriving the selection rules and represents the transition dipole moment. It is obvious the transition moment must be nonzero in order for a transition to occur.

Let us take a closer look at the transition moment function.

$$(\mathbf{m}_z)_{1,2} = \int \Psi_2^* \mathbf{m}_z \Psi_1 dt \quad (2.26)$$

This equation describes how “easy” the system can make a transition from state 1 to state 2, and is the key to determining selection rules [15]. The rotational level selection rules will be derived first. Assume the electric field lies only along the z-axis, and simply substitute equation 2.23 ($\mathbf{m}_z = m \cos(q)$) and the solutions of the rigid rotor model into equation 2.26.

$$(\mathbf{m}_z)_{1,2} = m \int_0^{2\pi} \int_0^\pi Y_{J'}^{M'}(\mathbf{q}, \mathbf{f})^* \cos(q) Y_J^M(\mathbf{q}, \mathbf{f}) \sin(q) dq d\mathbf{f} \quad (2.27)$$

where the dipole moment is pulled outside the integral, which directly shows there must be a permanent dipole moment present in order for the molecule to have a pure rotational spectrum [15]. The solution to the integral in equation 2.27 is only non-zero for values in which $J' = J \pm 1$.

The vibrational transition selection rule follows a similar path. It was stated above that only $\Delta v = \pm 1$ transitions are allowed. This is true for a first order approximation. First, recall the solutions to the nuclear portion of the harmonic-oscillator model are Hermite polynomials [15].

$$\Psi_v(q) = N_v H_v \left(a^{1/2} q \right) e^{-aq^2/2} \quad (2.28)$$

After applying the same substitutions as before in equation 2.26 the following results:

$$(\mathbf{m}_z)_{1,2} = \int_{-\infty}^{\infty} N_{v'} H_{v'} \left(a^{1/2} q \right) e^{-aq^2/2} \mathbf{m}_z(q) N_v H_v \left(a^{1/2} q \right) e^{-aq^2/2} dq \quad (2.29)$$

In order to solve the integral, the dipole moment must be expanded around the equilibrium nuclear separation. Including only the first-order term results in the $\Delta v = \pm 1$ selection rule. However, when the higher order terms are included in the dipole moment expansion, the allowed vibrational transitions are expanded to $\Delta v = \pm 1, \pm 2, \pm 3 \dots$ depending on how many nonlinear terms of the dipole moment expansion are included. The higher order terms are much smaller than lower order terms. This means that the bigger the Δv transition the more unlikely it is to occur [13].

In CO a $\Delta v = \pm 2$ is approximately 150 times more likely than a $\Delta v = \pm 3$. All $\Delta v > 1$ are called overtone transitions.

2.3 Thermal Population

In the previous theory section, the translational energy of the diatomic molecule was excluded. It was shown that the energy of a diatomic molecule can be written as a sum of the individual energies: electronic, vibrational, rotational, and now translational [14].

$$e_{Tot} = e_{elec} + e_{vib} + e_{rot} + e_{trans} \quad (2.30)$$

The translational energy is of particular interest because physical collisions between molecules cause quantum mechanical transitions. In other words, the collision between two diatomic molecules can cause a shift in the molecules' rotational level, inducing a rotational transition. These collisions which are responsible for the molecules' thermal distribution are described by the Boltzmann relationship,

$$F_s = \frac{g_s e^{\frac{-E_s}{kT}}}{\sum_j g_j e^{\frac{-E_j}{kT}}} \quad (2.31)$$

where F_s is the fraction of molecules, E_s is the energy, g_s is the degeneracy of state s , and the denominator is the summation over all energies [13]. Notice the Boltzmann relationship is a function of the Boltzmann constant times the temperature, which is approximately 190 cm^{-1} at room temperature. The approximate energy of a diatomic molecule associated with a vibrational transition is on the order of 2000 cm^{-1} . This

shows that almost all of the molecules at room temperature will be in the ground state. Rotational energy levels are spaced much more finely than vibrational levels, implying at room temperature there will be a thermal distribution of molecules throughout many rotational levels, Figure 2.4.

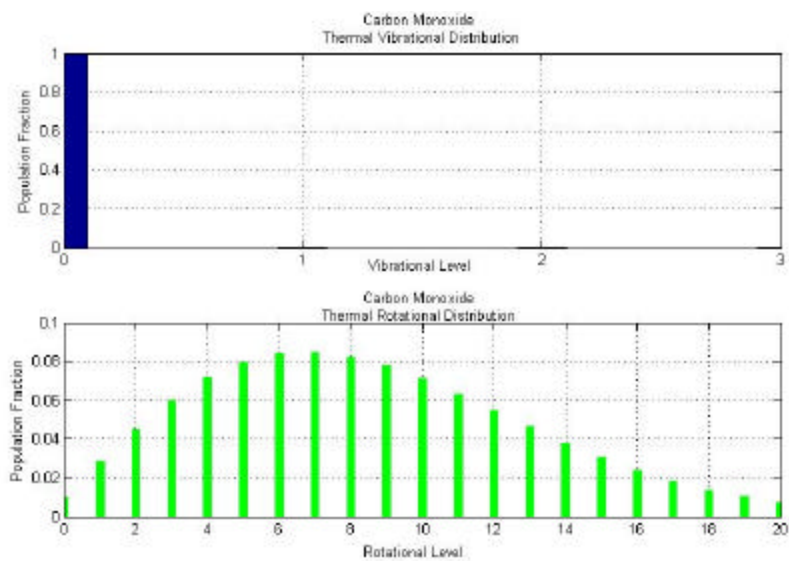


Figure 2.4. Vibrational and rotational distribution of CO at room temperature.

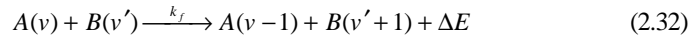
2.4 Kinetic Processes

This section will cover the various kinetic processes associated with optically pumped CO lasers. Rotational relaxation is the only process that occurs on the same

time scales as lasing. Vibrational-vibrational and vibrational-translational transitions occur on time scales much larger than the lasing processes. It will be shown in the numerical model chapter that V-V and V-T processes can be neglected for these experiments. Rotational relaxation is key to the scaling and efficiency of the CO optically pumped laser. Its major role is discussed in the radiative process section.

Vibrational-Vibrational (V-V) Transitions

V-V transitions occur when two molecules transfer vibrational energy among one another. Typically, one molecule transitions up a vibrational level and the other drops down a vibrational level.



Using the calculations from McCord (1999), the rate constant for V-V relaxation at room temperature is $k_f = 2.73 \cdot 10^{-12} \text{ cm}^3/\text{mole}\cdot\text{s}$. This leads to a V-V relaxation of 630 ns with 20 Torr of CO [4]. This is well beyond the lasing time scales of the CO cascade laser, which are on the order of 50-100 ns. The effect of V-V transitions in the numerical rate equation model will be shown to be negligible.

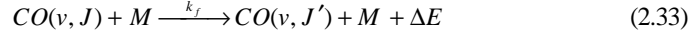
Vibrational-Translational (V-T) Transitions

V-T transitions imply a molecule imparts its vibrational energy to a collision partner in the form of translational energy. V-T is an extremely slow process, and with

a predicted relaxation time of 60 ms at 20 Torr of CO [4]. Thus, V-T is two orders of magnitude slower than the radiative processes in CO lasing and can be neglected.

Rotational-Relaxation (R-R)

R-R relaxations occur within the same vibrational manifold when two molecules collide. This results in a very small energy release and can be written as:



R-R relaxations occur on the same time scale as the CO radiative processes and must be accounted for in the rate equation model. The time scales of R-R will be explored in greater detail in a following section.

A qualitative discussion of R-R effects on the lasing properties of an optically pumped CO laser will follow. First, let us consider two cases of the R-R rates. Case 1 will represent near instantaneous R-R, and case 2 will assume a relatively slow R-R rate.

Absorption with Instantaneous R-R and Slow R-R Conditions

The near instantaneous, 1 ns, R-R case implies that a vibrational manifold will instantaneously reach the thermal Boltzmann distribution. The first benefit of instantaneous R-R is higher pump pulse absorption [17]. This is obvious by simply examining the laser gain/absorption equation.

$$g_{abs}(u) = s_{abs}(u) \left(N_U - \frac{g_U}{g_L} N_L \right) \quad (2.34)$$

This equation will be explained in much greater detail in the radiative process section, but for now we will quantitatively examine it. The $s_{abs}(\mathbf{u})$ is the absorption cross section, and can be treated as a constant for now. N_U, N_L are the populations of the upper and lower states respectively, and $\frac{g_U}{g_L}$ is simply a degeneracy term and can be assumed to be one for this discussion. The upper and lower states in this equation are rovibrational levels; they are specific rotational levels within a specific vibrational manifold. $g_{abs}(\mathbf{u})$ represents the absorption per centimeter of the incoming pump pulse. Notice once the upper state, N_U , reaches $\frac{1}{2}$ the population of the lower state, N_L , the pump pulse absorption goes to zero. This is termed saturation.

Now consider the case of slow R-R. This implies the pump pulse will remove molecules from a specific rotational level in the lower state and place them in a specific rotational level in a higher vibrational state. The population inversion will remain constant, and the transition will reach saturation quickly, since only the molecules in a specific rovibrational level can absorb the pump pulse.

Now imagine if the R-R process happened instantaneously. The lower rotational level would fill in from adjacent rotational levels as quickly as the pump removed them. This means N_L can now be considered the population of the entire lower vibrational manifold. The upper rotational level will relax out into adjacent states, spreading its population throughout the entire vibrational manifold in effect lowering N_U . This means the pump pulse can now pull CO molecules from the entire

lower vibrational manifold instead of a specific rovibrational level, and the upper rovibrational level never fills up. This allows for higher pump absorption, and greater efficiencies. One may question that if R-R is instantaneous and if the population inversion spreads out across the entire vibrational level, the gain must also decrease. This is true; however, the decreased gain is actually another benefit of instantaneous R-R.

Determining R-R Rate Constants

Phipps made the first direct measurements of CO-CO rotational relaxation constants using a double IR-IR pump probe resonance technique. The results of Phipps's research showed the statistical exponential power gap (SPEG) law produced the most accurate rate constants for CO-CO interactions [18]. The master equation governing the evolution of the rotational population in a specific v level is [19]

$$\frac{dN_J}{dt} = \sum_{J'} (k_{J \leftarrow J'} N_{J'} - k_{J' \leftarrow J} N_J) [CO] \quad (2.35)$$

where N_J is the population of the J^{th} level, and $k_{J \leftarrow J'}$ is the rate constant for the transition from the J' to the J level [19]. Assuming the thermal distribution of CO at room temperature only populates the first twenty rotational levels equation, 2.35 would require 400 rate constants to completely describe the system, and no experimental results contain enough information to determine each rate constant independently. The approach taken by Phipps is to solve the coupled differential equations 2.35 and compare the solution to the measured data. The rate constants used in the numerical

solution to equation 2.35 are generated from various state to state fitting laws. The SPEG law produced the best results with the least amount of error. The SPEG law is defined as

$$k_{J' \leftarrow J} = a_7 \left(\frac{\Delta E_{J'J}}{B_{v=3}} \right)^{-c_7} e^{\frac{-b_7 \Delta E_{J'J}}{KT}} \quad (2.36)$$

$$k_{J \leftarrow J'} = k_{J' \leftarrow J} \left(\frac{2J+1}{2J'+1} \right) e^{\frac{\Delta E_{J'J}}{KT}} \quad (2.37)$$

where $B_{v=3}$ is the CO rotational constant, $\Delta E_{J'J}$ is the energy gap of the transition, and the other coefficients are fitting parameters. The best fit parameters for the SPEG law determined by Phipps [19] were used in the rate equation model described later.

2.5 Radiative Processes

The three radiative processes developed by Einstein include spontaneous emission, absorption, and stimulated emission. All three processes describe a relationship between light and the population of the system's state [20]. Each process will be discussed in detail.

Spontaneous emission is the process by which an atom from state 2 spontaneously decays to state 1 with in a vacuum field. This, in turn, states that a system with an excited population will decay to the ground state through only spontaneous emission at a rate of A_{21}^{-1} . The spontaneous emission can be written as a simple rate equation.

$$\left. \frac{dN_2}{dt} \right|_{\substack{\text{Spontaneous} \\ \text{Emission}}} = -A_{21}N_2 \quad (2.38)$$

The energy must be conserved; therefore when the atom decays, a photon is released with the corresponding energy. The released photon is of random direction, phase, and polarization.

Absorption is the process in which an atom from state 1 absorbs a photon and excites the atom to the upper state 2. The photon energy must match the atomic transition energy:

$$\left. \frac{dN_2}{dt} \right|_{\text{Absorption}} = B_{12}N_1\mathbf{r}(\mathbf{n}) = -\left. \frac{dN_1}{dt} \right|_{\text{Absorption}} \quad (2.39)$$

where $\mathbf{r}(\mathbf{n})$ is the energy density per frequency interval. Notice the relation between the upper and lower states. As the lower state loses an atom the upper state gains an atom; and total population remains constant.

Stimulated emission is the main process within a laser medium. Stimulated emission is the result of a photon, generated from a transition, colliding with an atom in state 2, and causing the atom to drop to state 1 releasing another photon.

$$\left. \frac{dN_2}{dt} \right|_{\substack{\text{Stimulated} \\ \text{Emission}}} = -B_{21}N_2\mathbf{r}(\mathbf{n}) = -\left. \frac{dN_1}{dt} \right|_{\substack{\text{Stimulated} \\ \text{Emission}}} \quad (2.40)$$

The photon generated from stimulated emission must have the exact same frequency, polarization, direction, and phase of the incoming photon [20].

Einstein combined the three radiative processes under the framework of thermodynamic equilibrium to develop key relationships between the coefficients.

Basically, the combination of the three rate equations describes the system's population state at any given time.

$$\left. \frac{dN_2}{dt} \right|_{\text{Radiative}} = -A_{21}N_2 + B_{12}N_1\mathbf{r}(\mathbf{n}) - B_{21}N_2\mathbf{r}(\mathbf{n}) = -\left. \frac{dN_1}{dt} \right|_{\text{Radiative}} \quad (2.41)$$

This equation shows as state 2 loses an atom, state 1 gains an atom. Assuming equilibrium conditions and applying Boltzmann statistics, Einstein showed the following relationships between the radiative coefficients

$$g_2B_{21} = g_1B_{12} \quad (2.42)$$

$$\frac{A_{21}}{B_{21}} = \frac{8\pi h \nu^3}{c^3} \quad (2.43)$$

where $g_{1,2}$ is the degeneracy of states 1 and 2 respectively. The above relationships show that if one process is known, the others are also known [21].

2.6 Line Shape, Gain, and Absorption

The radiative processes involve photons of specific energies:

$$h\nu = E_2 - E_1 \quad (2.44)$$

where $E_{2,1}$ are the energies of the states 2 and 1 respectively. This implies an exact knowledge of the energy of an atom, which is impossible due to the uncertainty principle. This uncertainty results in a bandwidth or a distribution of energies around a central value when many atoms are considered in the system. This distribution is called the line shape, and its shape is influenced by many parameters.

Line Shape

The line shape function is defined as $g(\nu)$, and $g(\nu)d\nu$ is the probability a photon from the radiative processes will appear in the interval ν to $\nu + d\nu$ [21]. The same line shape function applies for all radiative processes. The line shape is considered broadened when the spectral width, $\Delta\nu$, increases. There are two types of broadening, homogeneous and inhomogeneous.

Pressure Broadening

Homogeneous broadening is caused by a mechanism that affects all atoms equally [21]. Pressure broadening is the most important homogeneous broadening effect and must be accounted for. Pressure broadening is a result of two molecules elastically colliding, which results in a discontinuous phase jump in the radiation [21]. The phase jump appears as broadening in frequency space. The collision rate of the molecules directly influences the pressure broadening effect. The more CO molecules that are present (higher pressure), implies more collisions which in turn broadens the line more. The same argument can be made for an increase in temperature and the addition of different gas species or collision partners. The FWHM of the pressure broadening is given by:

$$\Delta\nu_p = \sum s_i(T)p_i \quad (2.45)$$

where $s_i(T)$ is the temperature dependent pressure broadening coefficient for species i [MHz/Torr] and p_i is the partial pressure of species i . Pressure broadening, collision broadening, is represented by a Lorentzian line shape function,

$$f(\mathbf{n}) = \frac{Aw_L}{2p \left[(\mathbf{n} - \mathbf{n}_c)^2 + \left(\frac{w_L}{2} \right)^2 \right]} \quad (2.46)$$

$$w_L = \frac{NQ}{p} \sqrt{\frac{16kT}{pM}} \quad (2.47)$$

where w_L is the Lorentzian width, \mathbf{n}_c is the center frequency, A is the spectral area, N is the number density of the state, M is the reduced mass and Q is the collisional cross section [13].

Table 2.4. CO self-pressure broadening coefficients [22].

R(J)	Wavelength (nm)	Broadening (MHz/mBar)	R(J)	Wavelength (nm)	Broadening (MHz/mBar)
0	1573.7693	2.556	11	1565.3523	1.835
1	1572.8695	2.328	12	1564.7477	1.802
2	1571.9969	2.244	13	1564.1698	1.767
3	1571.1512	2.213	14	1563.6184	1.742
4	1570.3325	2.099	15	1563.0936	1.715
5	1569.5406	2.04	16	1562.5954	1.664
6	1568.7757	1.985	17	1562.1237	1.682
7	1568.0375	1.948	18	1561.6786	1.637
8	1567.3261	1.912	19	1561.2600	1.591
9	1566.6415	1.871	20	1560.8679	1.571
10	1565.9836	1.854			

Doppler Broadening

Inhomogeneous broadening pertains to the line broadening of different groups of atoms that are broadened differently. Doppler broadening is an inhomogeneously broadening process since it depends on the velocity of the gas flow. The velocity distribution can be represented by a Maxwell Boltzmann distribution, which in turn yields a Gaussian line shape,

$$f(\mathbf{n}) = \frac{A}{w_G} \sqrt{\frac{4\ln(2)}{p}} \exp \left[-4\ln(2) \left(\frac{\mathbf{n} - \mathbf{n}_c}{w_G} \right)^2 \right] \quad (2.48)$$

$$w_G = 2\mathbf{n}_c \sqrt{\frac{2RT\ln(2)}{Mc^2}} \quad (2.49)$$

where w_G is the Gaussian line width, \mathbf{n}_c is the center frequency, M is the molecular mass, T is the gas temperature, and R is the ideal gas constant [13].

Voigt Profile

At low pressures, 1-5 Torr, the line shape of CO can be represented by using a Gaussian profile. However, the majority of the laser experiments are at higher CO pressures, therefore pressure broadening can not be neglected. This forces the line shape to be a convolution of the Gaussian and Lorentzian line shape: a Voigt function.

The Voigt function is:

$$f(\mathbf{u}) = y_o + A \frac{2\ln 2}{p^{3/2}} \frac{w_L}{w_G^2} \int_{-\infty}^{\infty} \frac{e^{-t^2} dt}{\left(\left(\sqrt{\ln 2} \right) \frac{w_L}{w_G} \right)^2 + \left(\left(\sqrt{4\ln 2} \right) \frac{\mathbf{n} - \mathbf{n}_c}{w_G} - t \right)^2} \quad (2.50)$$

All the variables are the same as the Gaussian and Lorentzian line shapes. All line shapes mentioned above can be seen in ***Gain***

Assuming the radiant energy density spectral width is much smaller than the spectral width of $g(\mathbf{n})$, the radiative rate equation 2.41 can be written as:

$$\left. \frac{dN_2}{dt} \right|_{\text{Radiative}} = -A_{21}N_2 - \frac{\mathbf{s}(\mathbf{n})I_u}{h\mathbf{u}} \left[N_2 - \frac{g_2}{g_1}N_1 \right] \quad (2.51)$$

$$\mathbf{s}(\mathbf{n}) = A_{21} \frac{I^2}{8\pi n^2} g(\mathbf{n}) \quad (2.52)$$

where $\frac{I_u}{h\mathbf{n}}$ is the photon flux of the lasing transition and $\mathbf{s}(\mathbf{n})$ is the stimulated emission cross section with units of area. Typically the first term in equation 2.51, spontaneous emission, is dropped since it is very small compared to the stimulated emission.

Figure 2.5.

Gain

Assuming the radiant energy density spectral width is much smaller than the spectral width of $g(\mathbf{n})$, the radiative rate equation 2.41 can be written as:

$$\left. \frac{dN_2}{dt} \right|_{\text{Radiative}} = -A_{21}N_2 - \frac{\mathbf{s}(\mathbf{n})I_u}{h\mathbf{u}} \left[N_2 - \frac{g_2}{g_1}N_1 \right] \quad (2.51)$$

$$\mathbf{s}(\mathbf{n}) = A_{21} \frac{I^2}{8\pi n^2} g(\mathbf{n}) \quad (2.52)$$

where $\frac{I_u}{h\mathbf{n}}$ is the photon flux of the lasing transition and $\mathbf{s}(\mathbf{n})$ is the stimulated emission cross section with units of area. Typically the first term in equation 2.51, spontaneous emission, is dropped since it is very small compared to the stimulated emission.

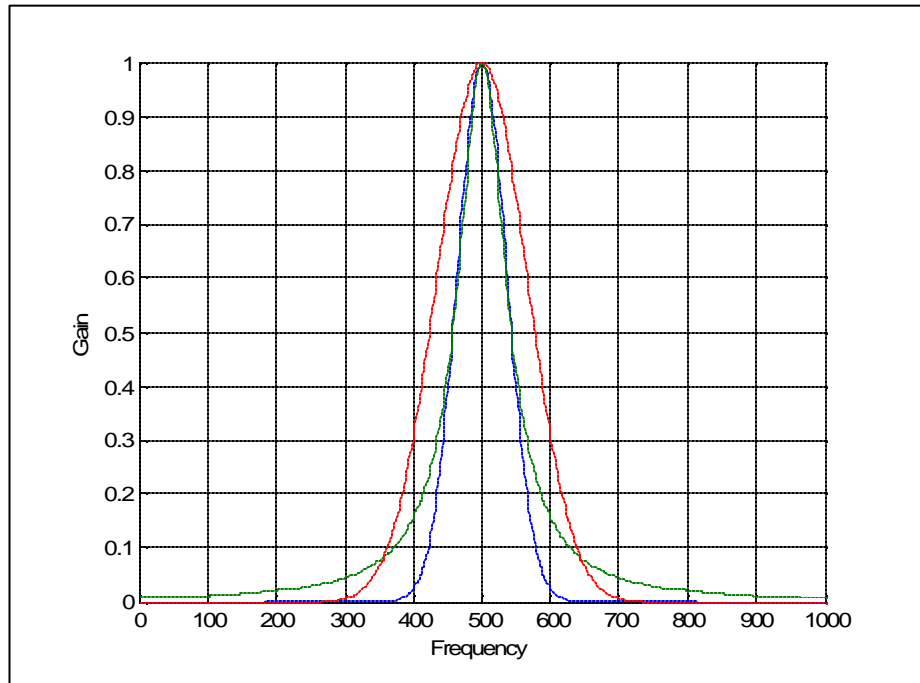


Figure 2.5. Lorentzian, Gaussian, and Voigt profiles. The Lorentzian profile (green) represents only pressure broadening, the Gaussian profile (blue) show only Doppler broadening effects, and the Voigt profile (red) is a convolution of both pressure broadening and Doppler broadening.

However, the spontaneous emission is very important since it is the starting process of a laser. The cross sectional area is the area of the atom visible to the photon flux [21]. Notice the absorption cross section depends directly on the Einstein A-coefficient. The A-coefficient is derived from a quantum mechanical approach, and it is directly related to the transition dipole moment which was discussed in section 2.2. As the transition becomes less likely (more forbidden) the transition dipole becomes smaller, resulting in a smaller cross sectional area. This simple statement defines the

largest obstacle in the 2nd overtone optically pumped CO laser. Since the pumped transition involves $\Delta v = 2$, it has a very small cross section. The small radiation absorption by the CO at the $\Delta v = 2$ wavelength is a direct result of the small cross section. Another interesting result of equation 2.51 is the fact that once the population of the upper state is equal to $\frac{g_2}{g_1} N_1$, the stimulated emission stops, in other words the laser's gain saturates.

Neglecting the spontaneous emission term and multiplying by the photon energy, $h\nu$, equation 2.44 can be written as:

$$h\nu \left. \frac{dN_2}{dt} \right|_{\text{Radiative}} = -s(\nu) \left[N_2 - \frac{g_2}{g_1} N_1 \right] I_\nu \quad (2.53)$$

The term on the left side represents the energy of a released photon times the rate of decay, and the right side term represents the changing intensity of the emitted photons. Since the photons released via stimulated emission are identical, the right hand side of equation 2.53 is the change of the radiated intensity with respect to distance through the system. The following results,

$$\frac{dI_\nu}{dz} = s(\nu) \left[N_2 - \frac{g_2}{g_1} N_1 \right] I_\nu = g(\nu) I_\nu \quad (2.54)$$

where $g(\nu)$ is the gain coefficient of the system, and I is the lasing intensity. It is obvious from equation 2.54 that a population inversion must be created in order for the optical system to have gain. The gain coefficient is written as:

$$g(\nu) = s(\nu) \left[N_2 - \frac{g_2}{g_1} N_1 \right] \quad (2.55)$$

Absorption: Beer-Lambert

Solving the differential equation 2.54 by integrating, results in the well known Beer-Lambert law.

$$g(n) = \frac{1}{L} \ln \left[\frac{I}{I_0} \right] \quad (2.56)$$

where I_0 is the initial intensity and I is the transmitted intensity. Replacing the gain coefficient in equation 2.56 results in the following:

$$N_1 = \left(\frac{g_2}{g_1} \right) \frac{s(n)}{L} \ln \left[\frac{I_0}{I} \right] \quad (2.57)$$

This simple equation states the number density of the lower state can be determined by measuring the absorption of incident radiation through a medium, where I_0 is the initial radiation intensity (before the medium) and I is the output intensity.

Amplified Spontaneous Emission (ASE)

Amplified spontaneous emission occurs in high gain laser systems as a result of the spontaneous emission being amplified by the same group of atoms [23]. The resulting pulse from ASE is semi-coherent and contains a large amount of energy. An ASE pulse will be spectrally coherent and have a moderate divergence which is acceptable for some applications. However, for the CO cascade laser, a highly coherent output beam is desired. Thus, ASE poses a problem. ASE radiation can become strong enough to cause saturation and to remove a significant portion of the

energy from the resonator by pulling atoms from the excited state down, which also results in a lifetime shortening [23]. The maximum gain allowed before ASE becomes a dominating factor is given by Verdeyen as,

$$G_0(n_0) - 1 = \frac{4pL^2}{A} \quad (2.58)$$

$$G_0(n_0) = e^{g_0 L} \quad (2.59)$$

where L is the gain length, A is the aperture area, and $G_0(n_0)$ is the power gain [24].

Equation 2.58 simplifies into an expression relating the gain to the ratio of the gain medium radius and gain length,

$$g_0 L = 2 \ln \left(\frac{2L}{a} \right) \quad (2.60)$$

where a is the gain diameter. It is easily seen from equations 2.58 and 2.59 that ASE is directly dependent on the gain of the system and the length to aperture ratio.

Laser Gain with Instantaneous R-R and Slow R-R

First, assume R-R is a slow process compared to the lasing time scales. This creates a huge population inversion between the pumped rovibrational level and the lower lasing level. Since all the inverted population goes to a single upper rovibrational level and the corresponding lower rovibrational population is zero. This can easily produce gains on the order of 1000% per centimeter [18]. Gain at such extreme levels produces a huge ASE pulse, which is not desired.

This is where instantaneous R-R comes into play. If the R-R is instantaneous then the excited rovibrational level will spread out to all rotational levels within the vibrational manifold based on the Boltzmann thermal distribution. This in turn distributes the gain to many rovibrational lines throughout the entire vibrational manifold in effect lowering the gain on any one specific lasing line to more reasonable levels. The laser will lase from the entire vibrational manifold from many rotational levels or from a single rotational level depending upon the resonator setup. All without ASE losses.

Through a quantitative discussion on R-R effects, it is obvious a fast R-R rate on order of ns or faster is desired. This provides many benefits to CO optically pumped lasers.

2.7 The Resonator and Cavity Modes

A simple stable curved-flat resonator was used for all experiments, and the theoretical discussion will center on the parameters of this resonator. The laser resonator provides positive feedback to the amplification loop, allowing a laser to oscillate.

Axial Modes of a Resonator

Axial modes occur in a passive resonator. They result from the phase matching conditions of a standing wave resonator after one round trip. This simply means the round trip length must be an integer number of wavelengths at the oscillating frequency [25]. The axial mode frequencies are easily calculated using the following equation:

$$\mathbf{n}_q = q \frac{c}{2L} \quad (2.61)$$

where q is an integer, and \mathbf{n}_q represents a set of frequencies oscillating in the optical cavity. The axial mode spacing is the free spectral range of the cavity.

$$\Delta \mathbf{u}_q = FSR = \frac{c}{2L} \quad (2.62)$$

The number of axial modes present in a resonator is a function of the resonator's free spectral range.

Transverse Modes of a Resonator

Transverse modes are the radiation intensity distribution in a cross-sectional plane perpendicular to the laser axis [26]. The simplest or lowest order transverse electric and magnetic mode (TEM) is the TEM₀₀. The TEM₀₀, commonly referred to as the fundamental mode, and has the intensity profile of a single Gaussian shaped dot. A laser will operate in all modes that have gain above the threshold level, so a typical laser will oscillate in multiple transverse modes. See Figure 2.6 for an intensity profile of higher order modes.

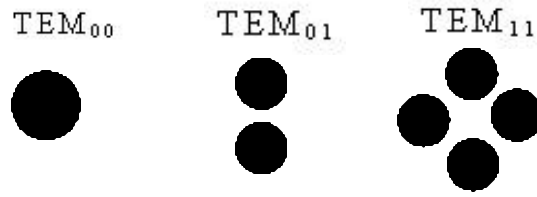


Figure 2.6. Transverse Mode Patterns.

Mode Spacing

A laser cavity oscillates on all the frequencies of the axial and transverse modes with gains above the threshold level. This typically results in many modes operating simultaneously and independently in the case of inhomogeneously broadened gain medium. Only the axial modes that have a gain above threshold will lase. There are 5 lasing modes in the above Figure. The mode spacing is given by:

$$\mathbf{n}_{q,m,n} = \frac{c}{2L} \left(q + (m+n+1) \frac{q}{2p} \right) \quad (2.63)$$

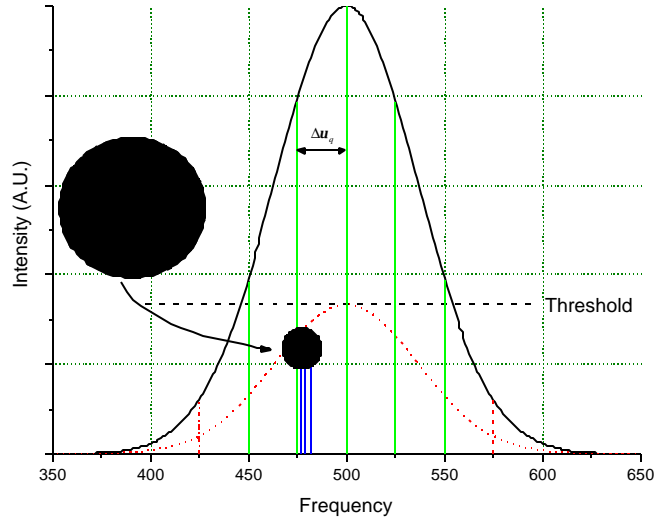


Figure 2.7. Mode spacing and allowed laser frequencies. The green lines represent the axial modes spaced by the resonator's FSR. The blue lines are the transverse modes.

$$\cos^2\left(\frac{q}{2}\right) = g_1 g_2 \quad (2.64)$$

$$g_{1,2} = 1 - \frac{L}{R_{1,2}}$$

where q is the axial mode index, m and n are the transverse mode indices, L is the cavity length, and $R_{1,2}$ are the resonator mirrors' radii of curvatures [27]. The relative spacing can be seen in Figure 2.7.

2.8 Mode Locking

Mode locking a laser is defined as locking the phase of all the axial modes together at a specific phase. For simplicity assume $\mathbf{f}_n = 0$. A very simple model of mode locking will be laid out in the following section; the model will predict the mode locked pulse width, pulse spacing, and peak power.

A very general expression for the total electric field in a resonator as a function of time is,

$$E(t) = \sum_{n=0}^{N-1} E_n \cos(2\pi \mathbf{n}_n t + \mathbf{f}_n) \quad (2.65)$$

where E_n , \mathbf{n}_n , and \mathbf{f}_n represent the amplitude, frequency, and phase of the n^{th} mode at time zero [28]. $E(t)$ contains the individual contributions of all the axial modes. Equation 2.65 assumes there is only one TEM₀₀ mode, which implies $\mathbf{n}_n = \mathbf{n}_0 + n\Delta\mathbf{n}_q$. Assuming each mode has the same amplitude allows E_n to be removed from the summation. This is obviously a gross approximation and assumes a square gain profile versus a Voigt profile. The time dependent intensity can be found by squaring equation 2.58.

$$I(t) = I_0 \left| \sum_{n=0}^{N-1} e^{i(2\pi \mathbf{n}_n t + \mathbf{f}_n)} \right|^2 \quad (2.66)$$

The plot of the intensity versus time is shown in Figure 2.8. By setting the phase term equal to a constant, $\mathbf{f}_n = 0$, forces a mode-locked condition in which the phase of each mode is the same.

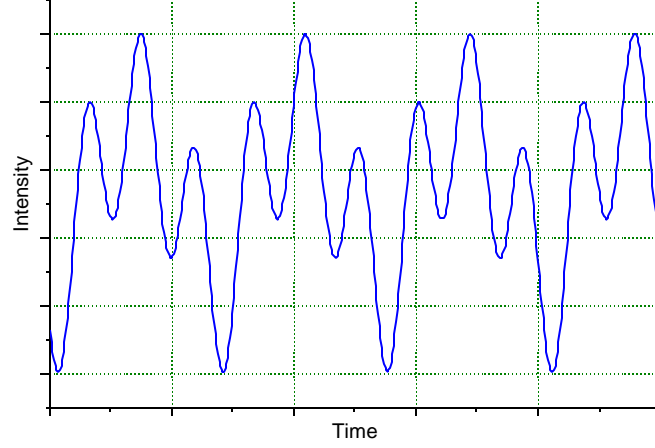


Figure 2.8. Plot of 4 modes oscillating with random phases.

The number of modes allowed to oscillate in a cavity depends on a few factors. First, the resonator length determines the axial mode space by equation 2.53. Each mode must lie within the gain profile, such that the maximum number of oscillating modes is

$$N = \Delta FWHM / \Delta n_q, \text{ where } \Delta FWHM \text{ is the full width half maximum of the gain profile.}$$

This assumes all the modes contained within the gain profile are above threshold. A square gain profile is not a good approximation of the gain profile; a better approximation is a Gaussian profile. In Figure 2.7 it is easily seen not all the modes under the Gaussian profile break threshold; thus only the modes within the FWHM of the line shape will lase. A simple expression for the number of modes assuming a Gaussian line shape is,

$$N = \frac{\Delta FWHM}{\Delta \nu_q} \left(\frac{\ln(K)}{\ln(2)} \right)^{1/2} \quad (2.67)$$

where K is simply the ratio of the threshold gain and the small signal gain, $K = g_0 / g_{th}$.

Using the new definition of the number of modes in equation 2.67 and assuming a locked phase, the following results.

$$I(t) = I_0 \frac{\sin^2(Np\Delta n_q t)}{\sin^2(p\Delta n_q t)} \quad (2.68)$$

As more modes are locked together the more intense and narrower each pulse becomes. Notice from equation 2.68 there are two ways to increase the number of modes in the laser system. First, the gain profile, $\Delta FWHM$, can be broadened allowing more modes to fit under the curve. The resonator can also be lengthened to decrease Δn_q . The FWHM of the mode-locked pulse is given by:

$$t = \frac{1}{\Delta FWHM \sqrt{\ln(K) / \ln(2)}} \quad (2.69)$$

Notice by increasing $\Delta FWHM$, the pulse width decreases; however by decreasing Δn_q the pulse width does not change. Figure 2.9 shows a pulse train of 4 and 8 mode locked pulses.

Figure 2.10 provides a rapid visual comparison between the Fourier transform of the 4 and 8 mode locked pulse trains. The beats can be described as axial mode beats and are separated by Δn_q .

The mode-locked pulse width in frequency space is also related to the Finesse of the cavity by:

$$d_n = \frac{\Delta n_q}{F}$$

$$F = \frac{p(R_1 R_2)^{1/4}}{1 - (R_1 R_2)^{1/2}}$$
(2.70)

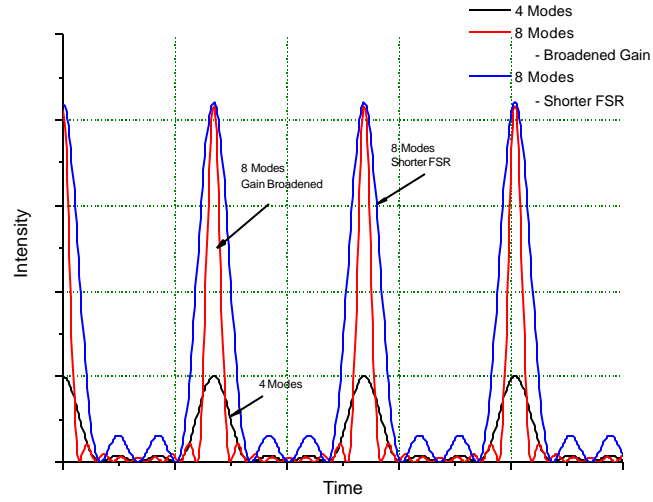


Figure 2.9. Intensity traces of mode locked pulse train for 4 and 8 modes. Notice the method used to increase the number of modes affects the pulse duration.

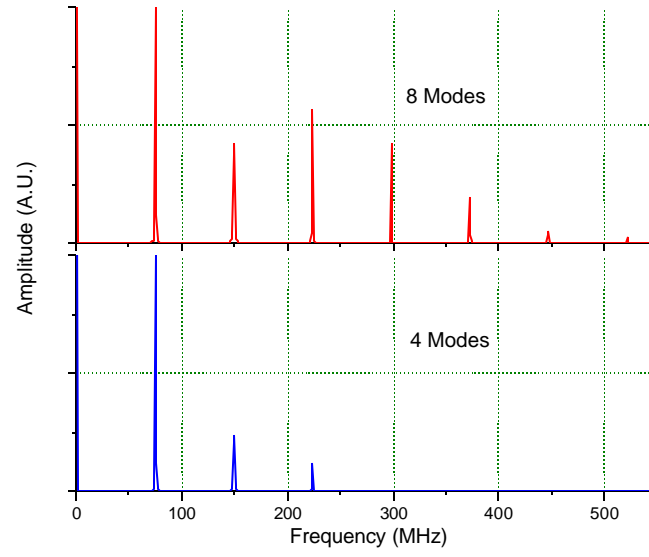


Figure 2.10. FFT of a mode locked pulse trains containing 8 and 4 modes respectively.

where F is the cavity Finesse and the R 's are the reflectivities of the resonator mirrors.

$$\Delta \mathbf{u}_r \text{ [29].}$$

CHAPTER THREE: EXPERIMENTAL AND PROCEDURES

This chapter outlines in detail all experimental components and procedures used to collect accurate and precise CO laser pulse data. The experimental setup is shown schematically in Figure 3.1. The OPO provided a tunable single mode pump pulse wavelength matched to specific rovibrational transitions in the 2nd overtone of CO.

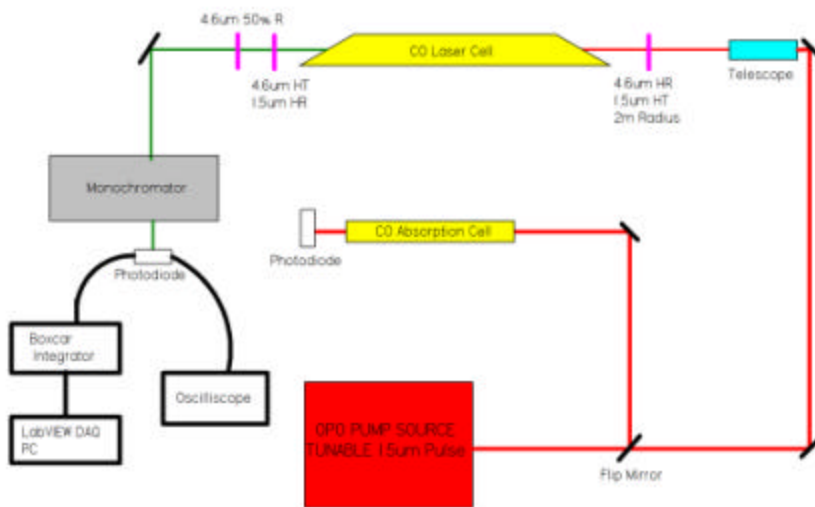


Figure 3.1. The top level experimental setup. The red line represents the 1.5 micron pump beam. The green line is the 4.7 micron CO laser pulse. The above setup provides a double pass pump run.

3.1 OPO Specifics

The optical parametric oscillator (OPO) was designed and manufactured by Aculight Corporation through a contract with the USAF. The OPO was used as the laser's pump source, providing 8ns, 10-20mJ pulses tunable between 1.55 and 1.58 microns. The OPO was wavelength tuned to match a specific rovibrational transition in the CO gas. A detailed schematic of the OPO is found in Figure 3.2.

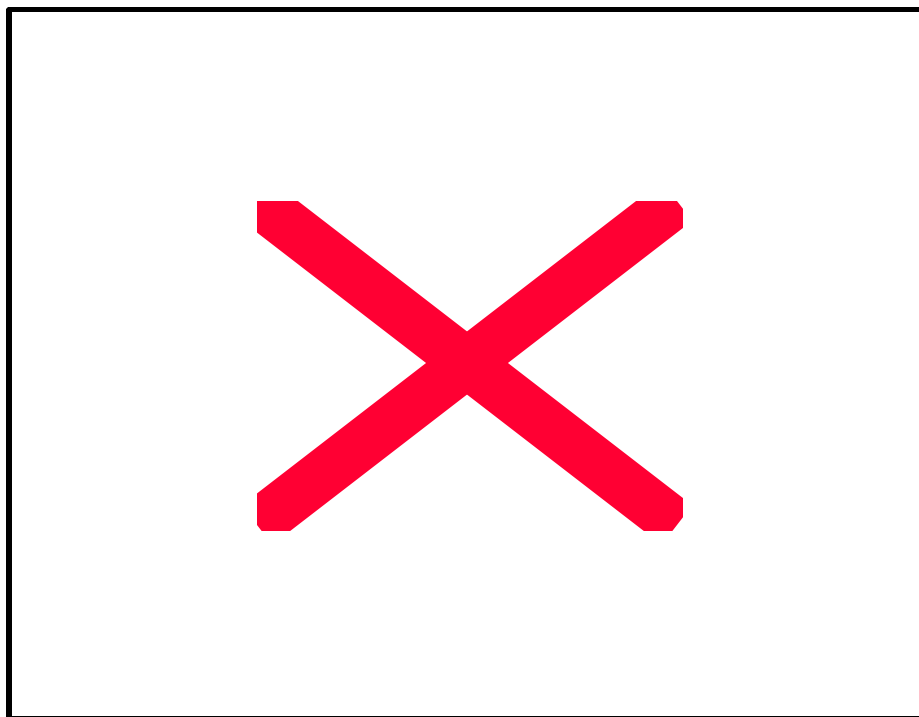


Figure 3.2. The OPO's setup. The black line is the 1064 nm seeded Nd:YAG pulse. The red line is the single mode tunable (1550-1580nm) continuous seed laser beam. The orange line is the narrow bandwidth pump pulse output from the OPO.

Nd:YAG

A Continuum Q-switched Nd:YAG provided the energy for the OPO resonator. The Nd:YAG was an injection seeded YAG, which allowed it to lase on a single axial mode. See Figure 3.3 for the seeded versus unseeded Nd:YAG operation. The Nd:YAG produced a 300 mJ pulse at a 10 Hz repetition rate with a pulse FWHM of 8 ns. The output pulse was periodically checked using various methods for correct seeder and resonator alignment to ensure the output was well seeded with a uniform transverse intensity profile. The first and simplest method used burn paper to view the beam's intensity profile. A more precise method employed a triggered infrared camera, Spiricon Pyrocam I. The Nd:YAG beam was highly attenuated and imaged onto the camera. The Nd:YAG alignment was tuned such that the output pulse's transverse intensity profile was Gaussian. The Nd:YAG laser did not have to be adjusted often, and remained well aligned for the majority of the experiments.

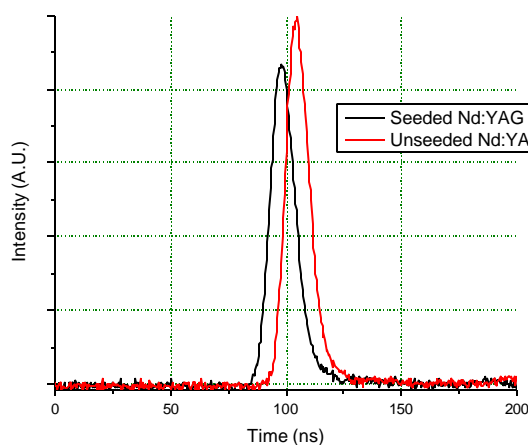


Figure 3.3. Seeded versus unseeded Nd:YAG operation. Notice the seeded pulse build-up time is shorter and the pulse is smoother.

The majority of the Nd:YAG pulse energy was dumped to avoid damage to the OPO optics using a half wave plate and a thin film polarizer. The Nd:YAG pulse was initially horizontally polarized as it exited the laser. Using a series of polarization selective optics, Figure 3.2, the Nd:YAG beam was selectively attenuated. A maximum of 150 mJ per pulse was sent into the OPO to avoid damage.

The attenuated beam diameter was reduced through a reducing telescope to 3 mm, which increased the intensity within the nonlinear crystal. The pulse's polarization was rotated to vertical orientation using another half wave plate just before entering the OPO resonator.

CW Diode Seed Laser

A tunable single mode laser diode, New Focus, was used to seed the OPO. The diode was tunable between 1.55-1.58 microns with an average output power of 7 mW. The seed laser passed through two Faraday optical isolators to protect the diode from unwanted optical feedback. The single mode operation of the New Focus diode was verified using a 6 GHz free spectral range etalon and an Indigo System's NIR camera. The beam was imaged onto the NIR camera after passing through the fixed etalon, and well formed rings were observed, indicating single mode operation. The New Focus control box also had a display indicating single mode operation.

OPO Wavelength Tuning

The OPO output pulse's wavelength was set by the seed laser's wavelength. The seed laser forced the OPO to lase on a single frequency due to pre-saturation of the gain. The seed laser's wavelength was set to a specific rovibrational transition energy, which are tabulated in Table 3.1. The $v(0,3)$ pump transition energies, wavelengths, and A coefficients for the CO rovibrational levels [30]-[31]. The Einstein coefficients were calculated using references [30] and [31]. A Burleigh WA-1500 Wavemeter was used to measure the seed laser's wavelength.

Table 3.1. The $v(0,3)$ pump transition energies, wavelengths, and A coefficients for the CO rovibrational levels [30]-[31].

Jlower	v = 0 to v = 3					
	R-Branch			P-Branch		
	cm ⁻¹	nm	A (Hz)	cm ⁻¹	nm	A (Hz)
0	6354.1717	1573.7693	0.0047	-	-	-
1	6357.8064	1572.8695	0.0057	6346.5869	1575.6500	0.0137
2	6361.3358	1571.9969	0.0061	6342.6372	1576.6312	0.0090
3	6364.7598	1571.1512	0.0065	6338.5828	1577.6397	0.0080
4	6368.0782	1570.3325	0.0067	6334.4238	1578.6756	0.0075
5	6371.2909	1569.5406	0.0069	6330.1604	1579.7388	0.0072
6	6374.3977	1568.7757	0.0071	6325.7927	1580.8295	0.0070
7	6377.3984	1568.0375	0.0072	6321.3209	1581.9478	0.0068
8	6380.2930	1567.3261	0.0074	6316.7452	1583.0938	0.0067
9	6383.0812	1566.6415	0.0075	6312.0656	1584.2674	0.0065
10	6385.7630	1565.9836	0.0076	6307.2824	1585.4689	0.0064
11	6388.3381	1565.3523	0.0078	6302.3956	1586.6982	0.0063
12	6390.8065	1564.7477	0.0079	6297.4055	1587.9555	0.0062
13	6393.1679	1564.1698	0.0080	6292.3121	1589.2409	0.0061
14	6395.4223	1563.6184	0.0082	6287.1157	1590.5545	0.0060
15	6397.5694	1563.0936	0.0083	6281.8163	1591.8963	0.0059
16	6399.6092	1562.5954	0.0084	6276.4142	1593.2664	0.0058
17	6401.5415	1562.1237	0.0086	6270.9094	1594.6651	0.0057
18	6403.3662	1561.6786	0.0087	6265.3021	1596.0922	0.0056
19	6405.0830	1561.2600	0.0088	6259.5924	1597.5481	0.0055
20	6406.6919	1560.8679	0.0089	6253.7806	1599.0328	0.0054
21	6408.1927	1560.5024	0.0091	6247.8667	1600.5463	0.0054
22	6409.5852	1560.1634	0.0092	6241.8509	1602.0889	0.0053
23	6410.8693	1559.8509	0.0093	6235.7334	1603.6606	0.0052
24	6412.0449	1559.5649	0.0095	6229.5143	1605.2616	0.0051
25	6413.1118	1559.3054	0.0096	6223.1937	1606.8920	0.0051
26	6414.0699	1559.0725	0.0097	6216.7718	1608.5519	0.0050
27	6414.9190	1558.8661	0.0099	6210.2487	1610.2415	0.0049
28	6415.6589	1558.6863	0.0100	6203.6246	1611.9608	0.0049
29	6416.2896	1558.5331	0.0102	6196.8997	1613.7102	0.0048

OPO Operation and Alignment Procedure

The details of the OPO will be covered first, and then the alignment procedure will be presented. The OPO cavity was a ring resonator design. See Figure 3.4 for a detail layout of the OPO resonator. The output coupler was a 1064 nm high transmitter and a 70 % reflector at 1550-1580 nm at a 22 degree angle of incidence. The seed laser was injected into the cavity through the output coupler, and only 30 % of the seed laser beam entered into the ring cavity. The back mirror, 1550-1580 nm high reflector, was mounted on a Melles Griot piezo-electric mount. The piezo mount allowed for quick and fine adjustments in the cavity length, and was controlled by an Aculight electronic locking circuit. The back mirror, high reflector, reflects 1550-1580 nm and transmits the 1064 nm pump pulse.

The cavity length fluctuated with room temperatures, air currents, and many other outside variables. The locking circuit monitors the 1.5 μm light that bleeds through from the high reflector, and in turn adjusts the cavity length through the piezo-electric mount. The bleed through was maximized by the locking circuit, which occurs when the total round trip cavity length is equal to an integer multiple of the wavelength. The better the alignment, the more intense the bleed through becomes.

Part of the OPO output was split off and directed through a 6 GHz etalon. The rings were imaged on to a CCD camera and observed on a television monitor. During single mode operation the rings were bright and well spaced. The rings did not fluctuate in intensity or position from pulse to pulse. When the OPO was misaligned,

not locked, or not seeded the nonlinear KTP crystal produced broad band 1.5 μm radiation. This was evident by dimmer, quickly shifting rings through the etalon.

OPO Alignment

The OPO alignment was broken down into two phases. First and most difficult was aligning the seed laser through the cavity. Second, the Nd:YAG pulse must be aligned to overlap the seed laser within the nonlinear KTP crystal. A series of carefully positioned apertures were used to map out the desired beam path, please reference Figure 3.4 for the aperture locations. The seed laser beam was roughly aligned through the apertures by adjusting the two seed laser alignment optics (see Figure 3.4).

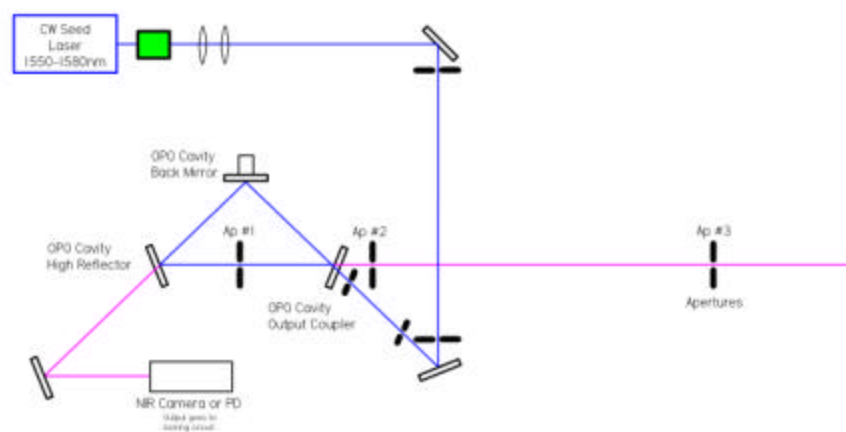


Figure 3.4. Blow up of OPO resonator. Notice the aperture and camera location.

The apertures forced the beam to travel in a straight and level path, and the correct angle through the cavity. A very sensitive InGaAs near infrared camera (Indigo

Systems Alpha NIR) was placed behind the OPO cavity high reflector. The seed laser injection optics were adjusted until the seed laser enters the ring cavity and passes through the aperture in the center and a circular diffraction pattern is visible on the InGaAs camera. The seed laser was now correctly aligned through the resonator. The output coupler was adjusted until the reflected portion of the seed beam travels through the two widely spaced apertures (AP#1 and AP#2 in Figure 3.4). The high reflector was adjusted such that the reflected beam traveled through the same widely spaced apertures. This guaranteed the ring resonator seed beam is traveling through the cavity on a straight and level path. The reflections from multiple passes were seen on the NIR camera, and the high reflector was adjusted such that all the reflections overlapped one another. The piezo voltage was manually adjusted causing fluctuations in the cavity round trip length. The voltage was tuned in such a manner that the cavity goes through various constructive and destructive interference lengths. The alignment was finely tuned to maximize the constructive interference visible on the NIR camera, see Figure 3.5.

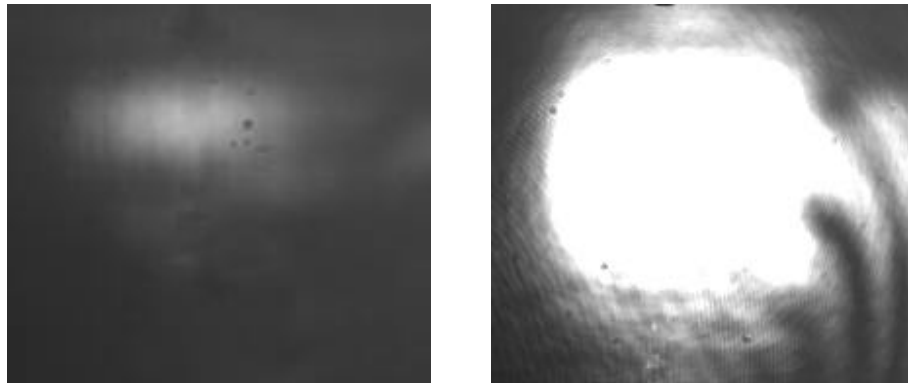


Figure 3.5. Aligned OPO bleed through. The typical beam profile display of the bleed through from the ring resonator for a minimized and maximized resonator length.

The Nd:YAG proved to be a much simpler process. The Nd:YAG pulse was simply aligned through the ring cavity such that it overlapped the seed laser beam. The Nd:YAG alignment was fine tuned once the OPO was thermally stabilized by tweaking the injection angle and position to maximized output power. The OPO was now nominally aligned.

The OPO Pulse

The OPO typically produced horizontally polarized 8 ns pulses with an average energy of 15 mJ at a 10 Hz repetition rate. The pulse energy was measured with a Gentec ED-200 joule meter and a Gentec Dou reader. The data is collected from the Dou meter using the manufacture's LabVIEW software. The vast majority of the Nd:YAG pulse went unused and simply passed through the cavity and was later discarded using a dichroic optic.

The OPO spatial beam profile was imaged using a Spiricon Pyrocam I infrared camera. The spatial profile varies greatly depending on the OPO cavity alignment. The beam quality did not affect the CO lasing, however the beam diameter did effect the lasing output of the CO. This was a direct effect of the pump beam volume that was incident on the CO cell. Since the pump pulse was far from saturating the transition, the same amount of CO molecules were excited with a large and small pump beam diameter. However, the number density of excited CO molecules, directly related to gain, is inversely related to the pump volume. So, if the pump pulse was focused

through the CO cell, very small beam radius, a large gain value would be achieved, which will be discussed further in the results section. Figure 3.6 shows a typical spatial profile of the OPO pulse. CO lasing was observed under a variety of pump pulse configurations; including collimated with a large radius (5 mm), tightly collimated with a radius of approximately 2 mm, and tightly focused in the center of the gain cell. The results and effects will be discussed in Chapter 4. Please see Figure 3.7 for a typical resonator and pump pulse setup.

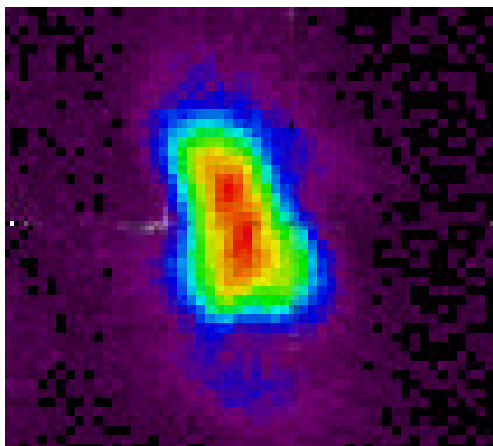


Figure 3.6. Typical spatial profile of the OPO pump pulse.

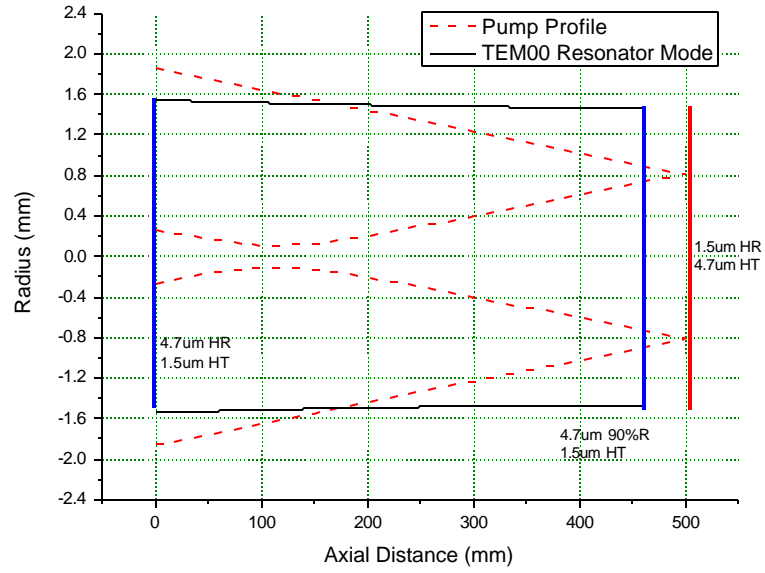


Figure 3.7. Short resonator with a double passed focused pump pulse. Notice the pump pulse slightly overfills the fundamental mode volume of the resonator on the second pass.

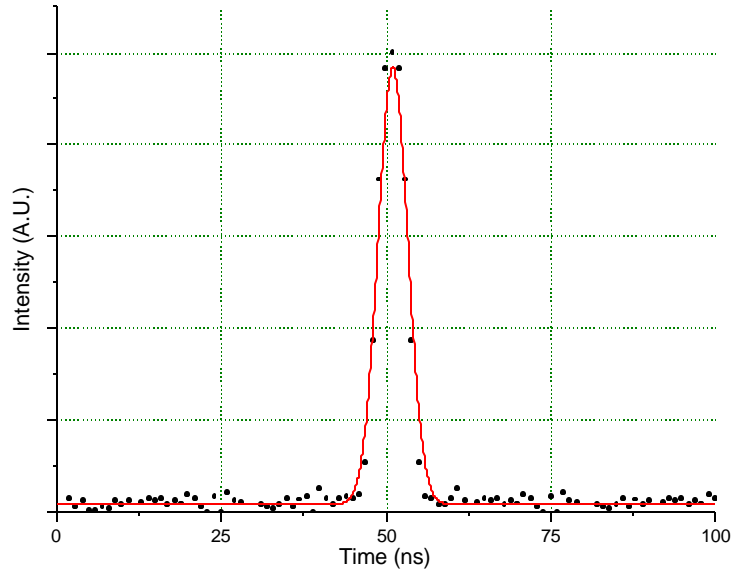


Figure 3.8. OPO temporal profile and bandwidth. The FWHM of the Gaussian fit is 6.0 ns which corresponds to a transform limited bandwidth of 166MHz.

The OPO pulse bandwidth, Figure 3.8, is determined by collecting the temporal profile of the pulse and computing the Fourier transform. The transform limited OPO pulse bandwidth is around 150 MHz.

OPO Operating Procedures

The OPO was a very sensitive optical system and required great care in setting its operating parameters and conditions. The Nd:YAG was cycled on first to a “flash only” mode allowing the flash lamps and rods to come to a thermal equilibrium. This warm up period was typically 45 minutes. While the Nd:YAG was warming up the rest of the electronics were cycled on, oscilloscopes, lock-in amplifier, and the piezo

controller. The New Focus diode was turned on, and the wavelength was adjusted to the correct transition wavelength. The diode also has a 30 minute warm up time according to the manufacture's manual. Thermal variations and differing air currents from day to day caused the OPO to misalign over time. The high reflector in the ring cavity was adjusted vertically and horizontally to re-maximize the constructive interference. This re-alignment was performed daily.

Once the warm up time is complete and the OPO is optimized the Nd:YAG is turned to Q-Switched mode thus producing high energy pulses. The OPO crystal is allowed to thermally stabilize for approximately 45 minutes before any adjustments are made. Once the KTP crystal was stable, the OPO was finely tuned to maximize the output pulse energy and pulse to pulse stability.

3.2 CO Lasing Cell

A 2 inch diameter stainless steel cell was used for most lasing experiments. The Cell has two CaF_2 on each end at Brewster's angle to maximize pump transmission. The cell length was adjustable between 29 and 45 inches. There are four ports on the cell used for CO filling and fluorescence measurements.

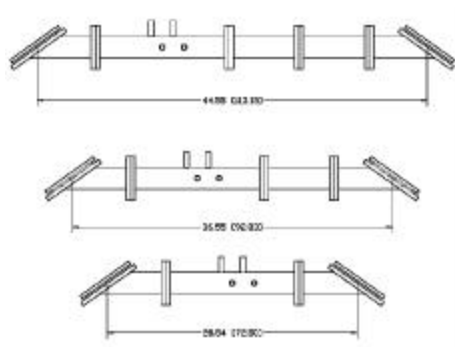


Figure 3. 9. Carbon Monoxide laser cell schematic.

Another cell was used for more flexible length adjustments. It was of the same design as Figure 3. 9 except the cell diameter was 1 inch, thus allowing a standard piece of stainless steel tubing to be inserted to adjust the length.

The cell was evacuated every test day to about 0.01 Torr using a Welch vacuum roughing pump. The cell was then flushed with research grade (99.99% purity) CO several times to ensure a low concentration of contaminants. This procedure was done daily to minimize contaminate gas effects. Two MKS Baratron (10 and 100 Torr) were connected to the cell to accurately measure pressures from 1 to 100 Torr. Both Baratrons were calibrated on a regular basis to a NIST traceable calibration stand by a certified technician. The cell leak rate measured 0.25 Torr/hour, and the cell was flushed through an experimental series to avoid contamination effects.

3.3 Photodetectors

Multiple photodiodes and photodetectors were used for the various experiments. There were three different wavelength regions of interest, 1064nm, 1550

nm, and 4.6 μm . A New Focus InGaAs 2033 large area photo receiver was used for all experiments that require measurement of the CW seed laser, such as the CO linewidth and absorption experiments. The New Focus photo detector has a 5 mm x 5 mm area and a 2 μs rise time. This detector was used because it implemented an internal gain circuit that produced an output signal on the order of volts which is easily read using a National Instruments DAQ break out board and A/D PCI card.

A ThorLabs DET110 InGaAs photodetector was used to accurately measure the temporal profile of a short pulse, such as the Nd:YAG pulse. The ThorLabs photo diode has a rise time of 5 ns, active area of 0.8mm x 0.8mm, and a spectral range from 700-1800nm. This detector was mainly used as a trigger and to measure the approximate temporal profile the Nd:YAG pulse.

Two Boston Electronics PEM-L photovoltaic detectors were used as the primary photodetectors for the CO laser pulse at 4.7 μm . The PEM-L was sensitive from 2-12 μm with a rise time of <0.5 ns. This detector proved to be sensitive enough to measure the CO laser pulse, and fast enough to for an accurate temporal profile.

A Gentec QE12SP joule meter was used to measure the energy of the 4.7 μm laser pulse. The QE12SP came with a manufacture's reported sensitivity to 7.0 μJ and a 3% uncertainty in power measurements.

A New Focus 1537 12GHz photo receiver was used to trigger the DAQ system, and obtain accurate temporal profiles of the OPO pulses. The photo receiver had a response time of 30 ps, and an active area radius of 25 μm .

3.4 Monochromator Operation

A Digikrom $\frac{1}{2}$ meter monochromator was used to spectrally separate the CO lasing output into the individual lasing lines. A green HeNe laser (540 nm) was used to calibrate and align the monochromator. The monochromator was controlled by a LabVIEW computer interfaced, Figure 3.10, and its operation was synchronized with the oscilloscope data collection.

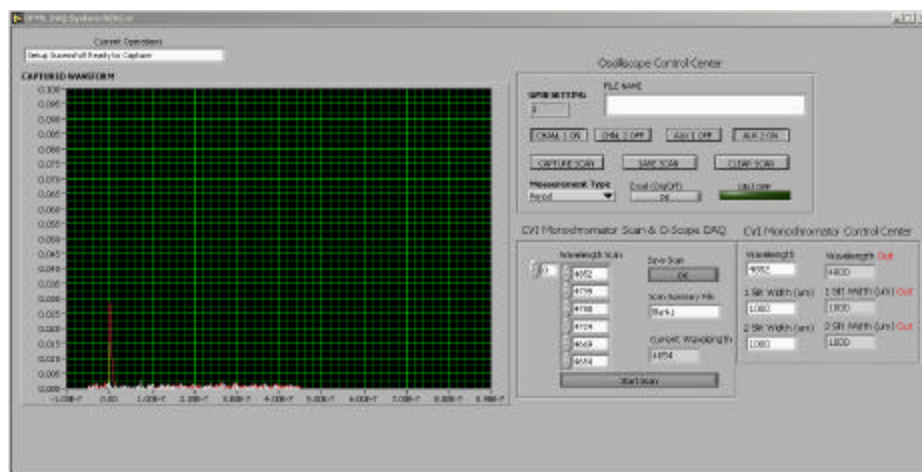


Figure 3.10. Screen shot of the data acquisition program. The LabVIEW program was used to control all the monochromator settings, and collect scans from the oscilloscope. The program would then compile the data from multiple wavelength scans and save the data in Excel format.

3.5 Data Acquisition: Oscilloscope

A Tektronix TDS 680B oscilloscope was used for the data collection from the various photo detectors. The TDS 680B had a 5 Gs/sec maximum sampling rate and a 1 GHz bandwidth.

The CO pulses were typically averaged over 5 waveforms to minimize shot to shot noise, and the data were sent to a computer using LabVIEW software and a GPIB interface. The data acquisition software displayed the plots on the screen allowing the user to view the collected plots before saving them to an Excel file.

The shot to shot variations depend directly upon the pulse stability of the OPO. The OPO was not very stable from shot to shot, but it did produce a stable output over 5 to 10 pulses, Figure 3.12. A Gentec Duo power meter provided the average energy over a user defined number of pulses. So, the average pump pulse energy is reported along with the average CO laser pulse data.

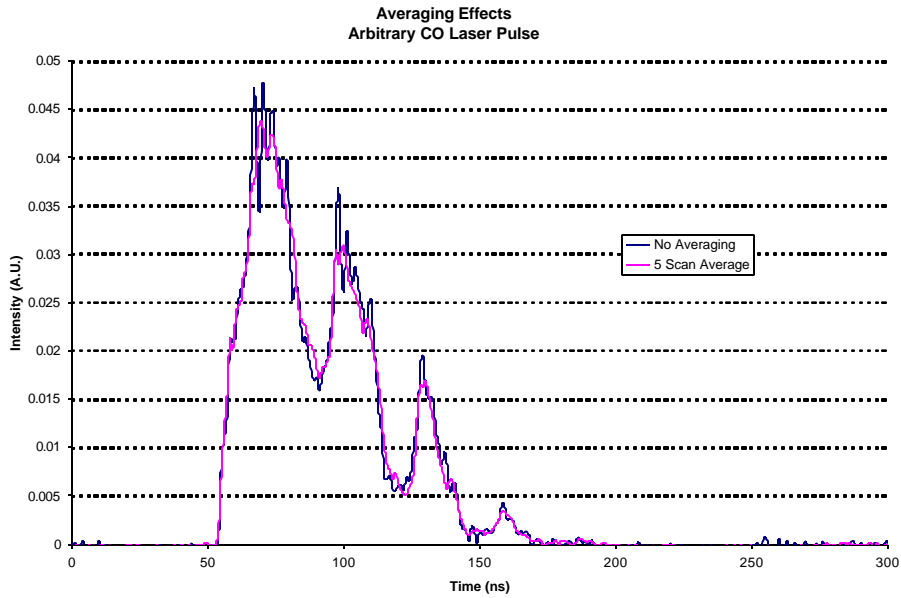


Figure 3.12. Averaging effects. The pink scan is an average of 5 scans, and the blue trace contains no averaging. Average effects were considered through out the experiment and were considered negligible.

CHAPTER FOUR: RESULTS AND DISCUSSION

This chapter gives the details and results of the CO lasing experiments, and the theoretical modeling.

4.1 Lineshape Analysis and Pressure Broadening Coefficients

The 2nd overtone absorption lineshapes of CO were measured using the tunable diode laser over range of pressures, from 0-100 Torr. The experimental data agreed within 15% of the published data by Henningsen [22]. The difference can be explained by systematic errors in the experiment, such as using a non optimized Fabry Perot interferometer to calculate the frequency scan range of the diode. The interferometer was originally coated for wavelengths ranging from 1.1 μm to 1.3 μm , and the finesse suffered greatly at 1.5 μm . This created a large uncertainty in the frequency calibration of the laser scan. A simpler less stringent method was used to fill the CO cell than that of Henningsen, possibly resulting in a higher contaminate ratio. However, regardless of the experimental error a good agreement between published results was obtained, Table 2.4. See Figure 4.1 for a sample of the fitted lineshape function at 10 and 100 Torr of CO.

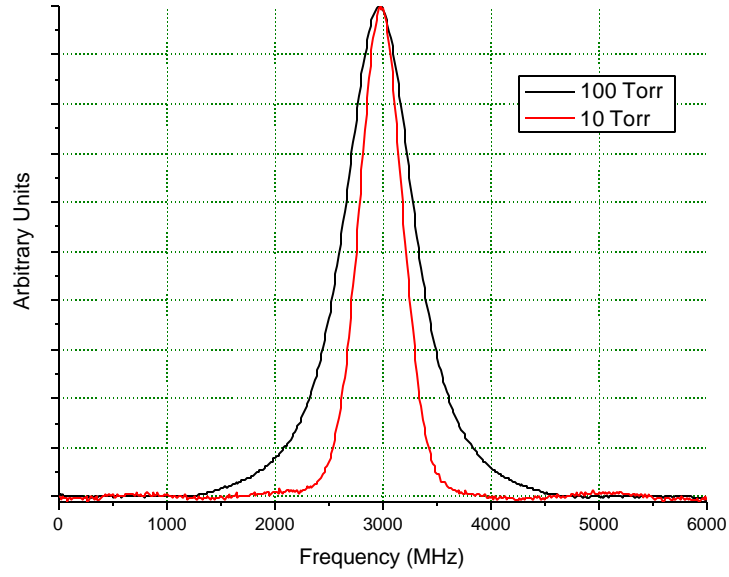


Figure 4.1. The lineshapes of $\nu(0,3)R(8)$ transition at 10 and 100 Torr of CO with pressure broadened linewidths of 260MHz and 26MHz respectively.

4.2 CO Lasing Results Short Gain

The results of a short gain medium, 33cm, will be covered in this section. The effect of CO pressure, output coupler transmission, and resonator length were measured for the $\nu(0,3) R(6)$ pump transition, as shown in Figure 4.2.

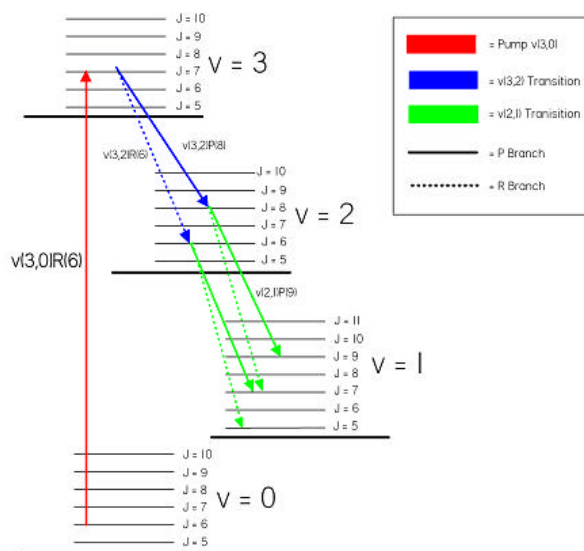


Figure 4.2. Energy level diagram of pumped transition.

A stable resonator with a 45 cm gain length, a high reflector with a 5 m radius of curvature, and a flat output coupler with reflectivities from 10-95% were used for this series of experiments. The resonator parameters for the short cavity can be found in Figure 4.3.

Notice in Figure 4.3 the pump beam will excite CO outside of the fundamental mode volume thus inducing higher order transverse mode lasing. The multi-mode lasing caused an extreme sensitivity on the photo detector location, since the detector would pick up different mode beats and entirely different modes based on its location. This resulted in a strange temporal profile of the CO laser pulse. This phenomenon was observed in the data sets, and can be explained by transverse mode beats. Two data

sets were collected along with the 4.7 μm beam profile. In both data sets the laser ran in multimode operation, but the resonator was misaligned in the

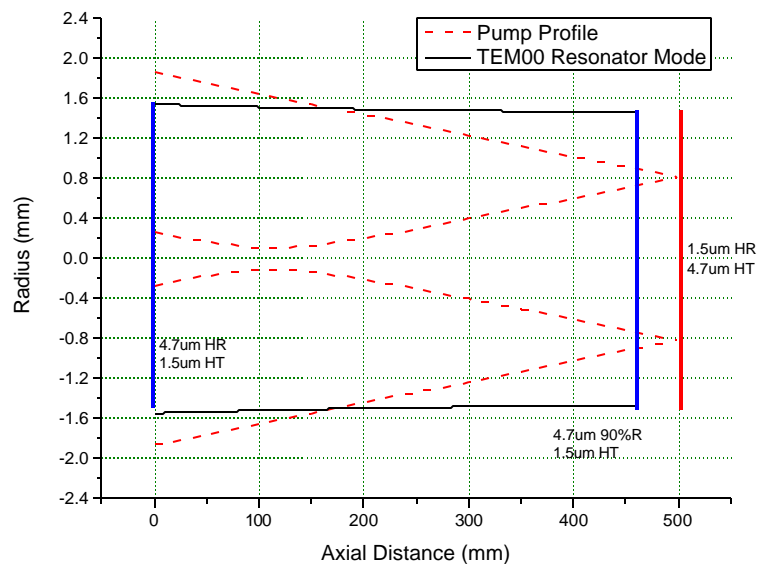


Figure 4.3. Fundamental resonator mode and pump pulse. The blue lines represent the resonator optics, and the solid red line represents the double pass optic.

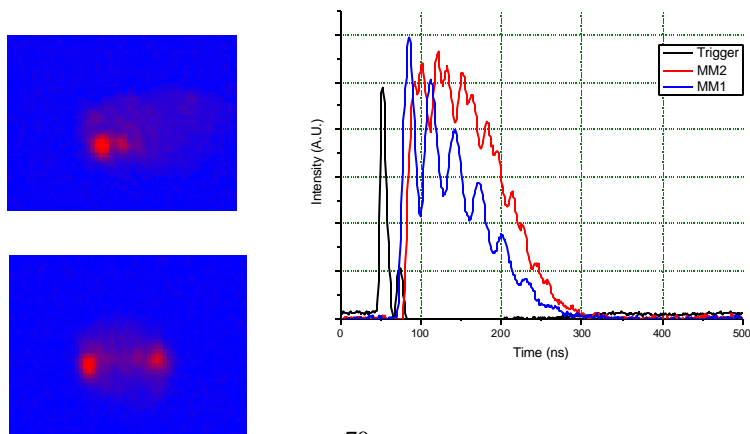


Figure 4.4. Multi-transverse mode lasing. The red line, MM2, corresponds to the bottom beam profile, and the blue line corresponds to the top beam profile.

second data set to allow for higher order mode oscillation, as shown in Figure 4.4.

The red line, in Figure 4.4, has a secondary beat frequency that is absent from the blue line, due to more transverse modes running. A qualitative estimate of the modes running in each case can also be inferred from the beam profiles in Figure 4.4. The fast Fourier transform, FFT, of MM1 and MM2 (Figure 4.4), was taken to determine the beat frequencies more accurately. The beats line up with the transverse mode frequency spacing between the fundamental mode and the TEM_{01} and TEM_{11} that were calculated using equations 2.62 and 2.63.

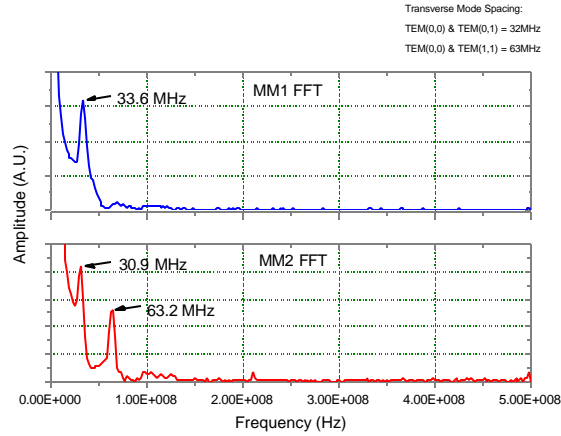


Figure 4.5. FFT of the multi-mode CO laser pulse. The beat frequencies occur at the two transverse mode beats.

The CO laser was forced to run in single mode operation simply by placing an adjustable aperture within the resonator and which filtered out all higher order modes. Figure 4. 6 shows a plot of a unapertured resonator and an apertured resonator. The oscillations are no longer present under the single mode operation since only one mode exists and there are no beats. The mode beating effects are evident in most of the short gain data sets.

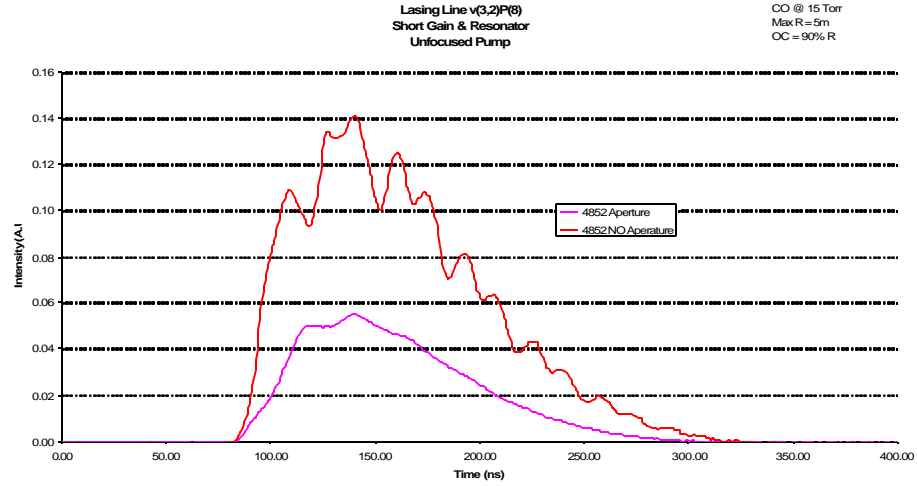


Figure 4. 6. Multimode and single mode operation. The laser was forced to run in the fundamental mode by aperturing out all other modes in the resonator.

Data was collected using two pump configurations, focused pump and unfocused pump. The focused pump's beam profile is displayed in Figure 4.3, and the unfocused pump maintained an average beam diameter of 6 mm throughout the gain region. The gain was calculated based on the percentage of the pump absorption and the mode volume of the pump. The gain volume was calculated as the product of the gain length and the cross-sectional area of the pump mode. The absorption of the pump pulse

proved to be very difficult to measure due to fluctuations in pump pulse intensities and the very small absorption cross-section of the 2nd overtone. The absorption was measured experimentally by simultaneously using two Joule meters. The first energy meter measured a portion of the pump pulse not transversing the CO cell, and the second energy meter measured the power transmitted through the cell. The ratio between these two powers any noise from pump pulse fluctuations. The CO cell was then filled with various pressures of CO and the ratios were compared to that of the empty cell. The results are shown in Figure 4.7.

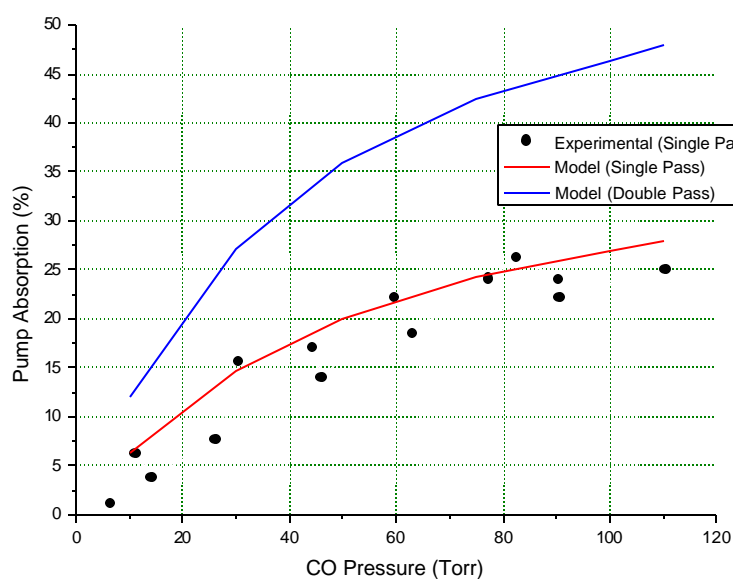


Figure 4.7. Pump absorption versus CO pressure through a 1.82m static CO cell. The absorption curves above are for the $v(0,3)R(6)$ transition at 1567.77nm.

The gains at 30 Torr of CO for the focused and unfocused pump profile was estimated to be around 150 % cm^{-1} and 30 % cm^{-1} respectively, with out taking into account any loss from R-R. The huge difference in the gains was due to the squared dependence of gain on the pump radius. Under the focused pump conditions the high gain results in an ASE pulse allowing the CO to lase without any resonator optics. A typical set of spectrally resolved plots are shown in Figure 4.8. Some salient observations were made, such as the mode build up times between the focused and unfocused pump pulse. The focused pump pulse has a mode build up time of 5ns and was coincident with the pump pulse. This was evident of the fact that the CO was super radiant under the same conditions. The unfocused pump case had a mode build up time on the order of 15ns, and was not super radiant, Figure 4.8. The value agrees with the results from the analytical representation of the mode build up time [5]

$$t = \frac{d}{cLa} \ln(ALN_u \mathbf{d}) \quad (4.1)$$

where d is the resonator length, L is the gain length, \mathbf{a} is the small signal gain, A is the mode area, and \mathbf{d} is used to represent the fractional change in gain ($\mathbf{d}=0.1$).

Equation 4.1 was used to determine the mode build up time based off of the calculated gain, and also to calculate the gain from the measured mode build up time. The numerically estimated mode build up times for 30 Torr of CO the unfocused pump is 16.2 ns. This number agrees very well with the experimentally determined value of 14 ns (unfocused). Equation 4.1 was solved for gain and the upper state number density simultaneously using the measured mode build up times. Gain calculated from

equation 4.1 for the unfocused pump was $10 \% \text{ cm}^{-1}$. This compares well with the gain calculated based on the pump absorption and pump beam area, $7 \% \text{ cm}^{-1}$. Cascade lasing, lasing from the $v(3,2)$ and $v(2,1)$ levels, was not seen under any resonator configuration or CO pressure for the unfocused pump pulse. This behavior was simply a result of the much lower gain. Population inversion initially starts on the 2nd overtone and it lases to the 1st overtone level. Inversion on the $v(2,1)$ line was created by the radiative stimulated emission from $v(3,2)$. However, the initial inversion is split by the P and R branch lasing lines to two separate rotational levels in the 1st overtone band. This result effectively implies the inversion on the $v(2,1)$ transition is at best $\frac{1}{4}$ of the initial

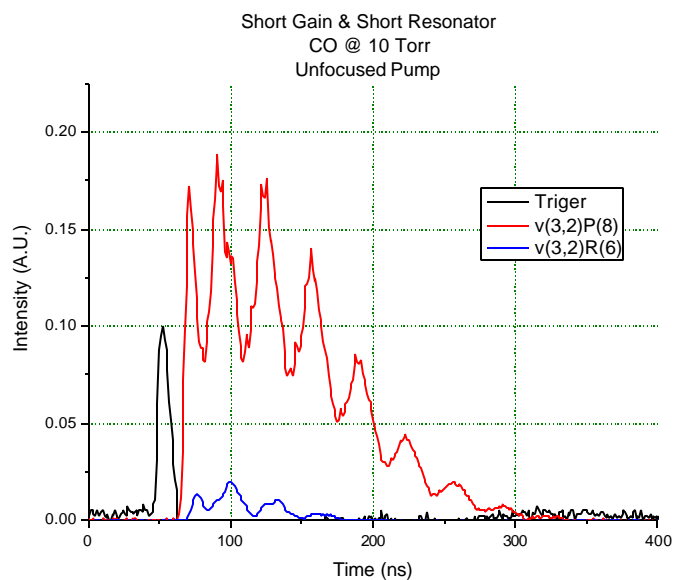


Figure 4.8. A typical plot of the spectrally resolved CO laser pulse. The oscillations are described as transverse mode beats. The lasing only occurred on the 2nd overtone band. This data represents an unfocused pump pulse with a gain on the order of 30 % cm^{-1} .

inversion. The smaller inversion of the 1st overtone level causes the gain to be below the threshold, and stimulated emission never begins. The short gain cell condition was not investigated in great detail because it was far from an optimized condition. A very small fraction of the pump pulse was absorbed in the small gain length. It was used to experimentally show that under a long resonator and long gain cell conditions, on the order of 2 meters, the CO laser self mode-locks. Since the FSR of the short resonator is on the order of 270 MHz and the lasing transition's

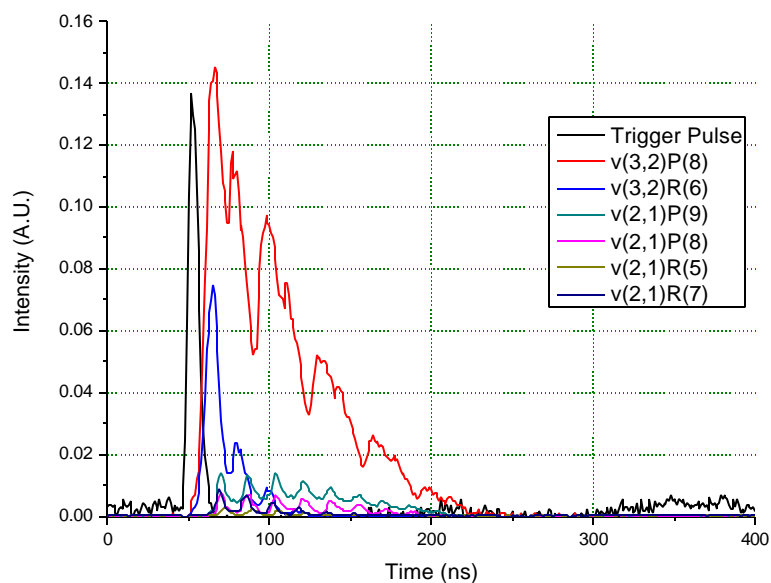


Figure 4.9. Typical plot of the spectrally resolved CO pulse under the focused pump transition. The gain is much higher under these conditions, and cascade lasing is evident (short cell).

FWHM is also on the order of 270 MHz only one axial mode would be present. This would eliminate the CO laser's mode-locking capability due to the lack of multiple modes.

4.3 CO Lasing Results Long Gain

A long gain cell of 2.0 m was used for the vast majority of the data collection. Under the long gain cell a variety of conditions were studied. An unexpected result occurred with the long gain cell and a focused pump beam geometry, the CO laser self mode-locked.

The CO was super radiant under these conditions and did not require a resonator to emit a semi coherent pulse. The most interesting part was that the super radiant pulse acted as an injection seeder and forced the CO laser to mode-lock, Figure 4.10.

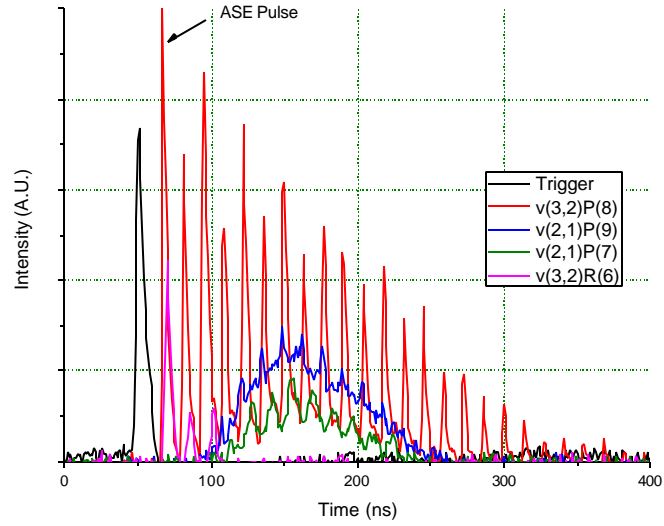


Figure 4.10. Mode-Locked pulse train.

The $v(3,2)P(8)$ lasing line has a FWHM of 400 MHz at a CO pressure of 75 Torr, and the resonator had a full spectral range of 74 MHz. This implies approximately 5 axial modes are resonating within the cavity if a highly reflective output coupler, 95% reflective, is used. The pulse widths are related to the number of modes locked together by equations 2.68. The estimated pulse width of 5 ns agrees with the measured pulse width of 5 ± 1 ns.

The mode-locked pulse train's frequency spectrum also correlates very well with the experimentally determined values.

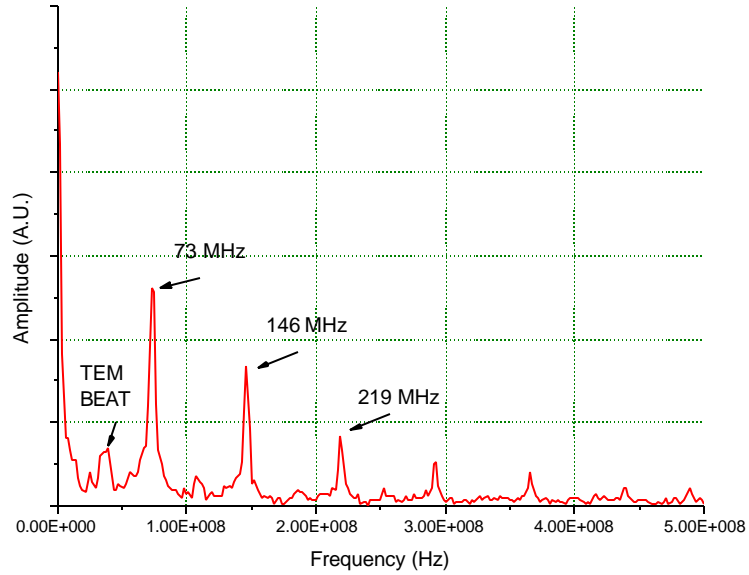


Figure 4.11. The FFT of the mode-locked v(3,2)P(8) laser line.

The beat frequency spacing of 73 ± 4 MHz multiplies corresponds to the FSR of the laser cavity, Figure 4.11. TEM beat frequency can also be seen in Figure 4.11, and corresponds to the beat frequency between the TEM_{00} and TEM_{01} modes. The number of modes oscillating can also be inferred from Figure 4.11 as 5 modes. This agrees well with the longitudinal mode spacing and the approximated bandwidth of the lasing transition, 400 MHz.

The mode-locking operation was evident only under the focused pump conditions, higher CO pressures, and a high reflectivity output coupler. The high output coupler's reflectivity lowers the threshold gain level, and allows for more axial modes to break threshold. The focused pump condition increased the gain which also allows for more axial modes to break threshold. The higher CO pressures broadened

the CO lasing line spectral width, again allowing more axial modes to fit within the gain profile.

The next series of experiments were designed to maximize the CO laser power output, and efficiency. A long gain cell, 182cm, was used along with a long resonator, 233 cm. Specifications for this series of experiments can be found in Table 4. 1.

Table 4. 1. Experimental specifications for lasing experiments.

CO Laser Specifications	
Gain Length	182 cm
Resonator Length	233 cm
Cavity Round Trip	15.5ns
Cavity FSR	64.4MHz
MaxR	98% R
Radius of Curvature	500 cm
Pump Transition	v(0,3)R(6)
Pump Wavelength	1568.77nm

The pump pulse was double passed through the static CO cell. Various CO pressures, pump beam profiles, and output coupler reflectivities were explored. The pump beam geometry used to produce the maximum power was a tightly collimated pump pulse with an average beam waist of 1.89 mm through the gain region including the double pass. ASE was present under the optimized pump profile; however it was not as dominating as under the focused conditions. Mode-locking was also less prevalent in the optimized geometry. It appeared as though the CO laser was running only in the fundamental transverse mode, since no transverse mode beat frequency appeared in the data and the pump was mode matched to the fundamental mode, Figure 4.12. However, this was not experimentally confirmed.

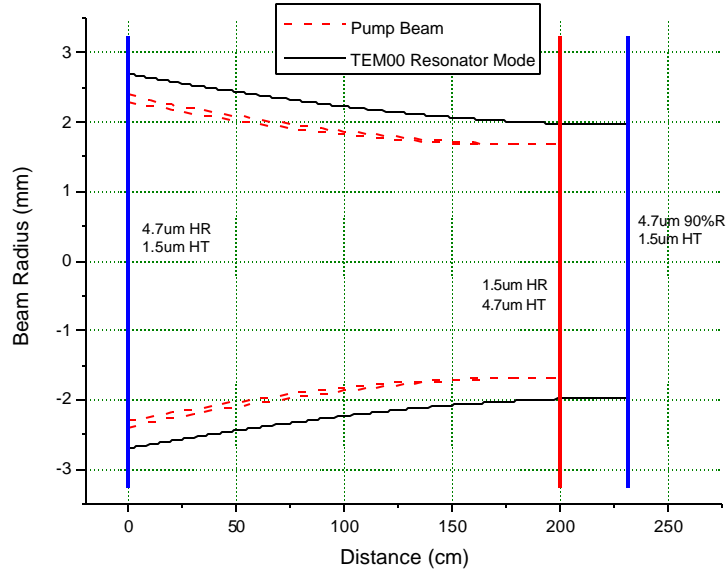


Figure 4.12. Long cavity resonator fundamental mode volume. It is easily seen that the pump beam creates gain only within the cavity's fundamental mode volume. This implies the CO laser is running in single mode operation.

The CO pressure had a large effect on the temporal behavior of the CO laser pulse, Figure 4.13. At lower pressures the CO lased for a much longer period of time, but with lower peak intensity. This observed behavior can be explained by the RR, VV, and VT effects that start to come into consideration at higher CO pressures. As the pressures become higher the kinetic effects' time scales decreases to that of the lasing time scales. All the above kinetic effects decrease the population inversion with time, thus lowering the gain. The initial spike that overlaps with the pump pulse is the ASE pulse, which is larger at lower pressures. The gain calculated from the absorption and mode build up time was estimated to be $22 \pm 1 \text{ \% cm}^{-1}$. The optimized pressure was

found experimentally to be between 40 and 50 Torr of CO for all the output coupler reflectivities. The CO laser

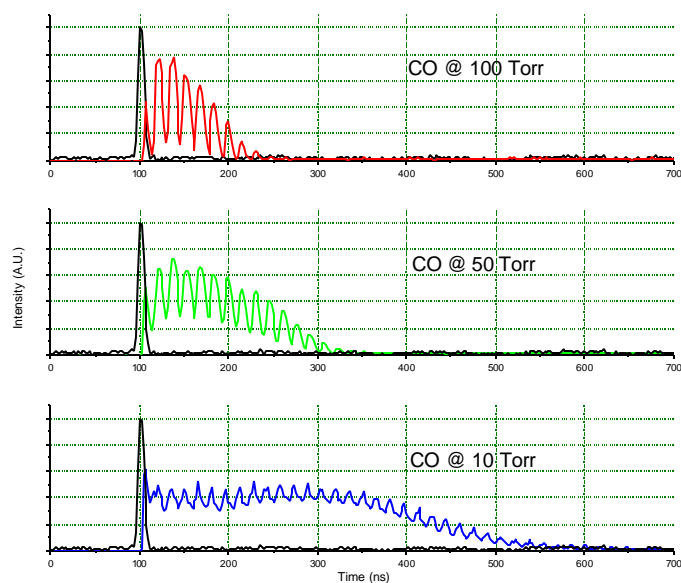


Figure 4.13. CO laser pulse out with a 70% R output coupler under various CO pressures.

pulse was spectrally resolved through a monochromator, and various lasing lines were observed. The CO did not lase on the $v(2,1)$ transition at higher pressures, above 20 Torr. This was due to the RR and VV decreasing the gain on the specific transition. Spectrally resolved lasing transitions with a 70% reflective output coupler can be seen in Figures 4.14-15 at various CO pressures. At pressures above 20 Torr no cascade lasing was present. Please see Appendix A for the plots of all the data collected.

An intensity saturation curve was collected by measuring the CO laser pulse energy versus output coupler transmission, the results can be seen in Figure 4.16. The

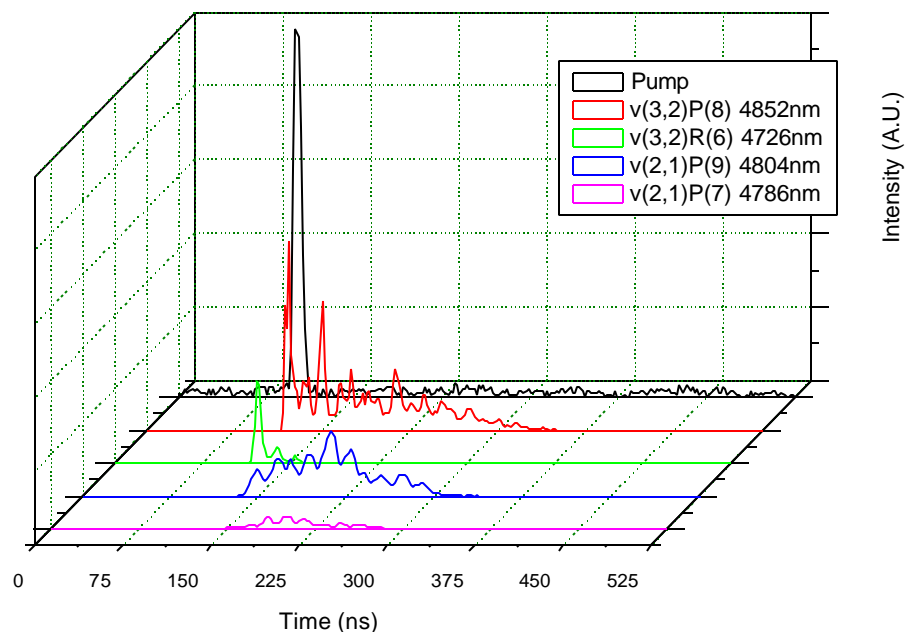


Figure 4. 14. Figure 4.14. Spectrally resolved lasing output with a 70% reflective output coupler, and 10 Torr of CO. There are two lasing lines from the v(3,2) both the P and R lines, and two v(2,1) only the P lines.

Rigrod analysis was applied to the collected Isat curves, however the results have very limited accuracy due to several reasons. First, the Rigrod analysis assumes continuous wave operation which is far from the experimental setup. Since, the pulse width is on the order of 6ns and the cavity round trip time is around 15ns the pump pulse does not engulf the entire cavity at one time, rather it rattles back and forth. This causes the gain change spatially and temporally. Also, the Rigrod analysis does not take into account ASE, which also affects the accuracy of the prediction.

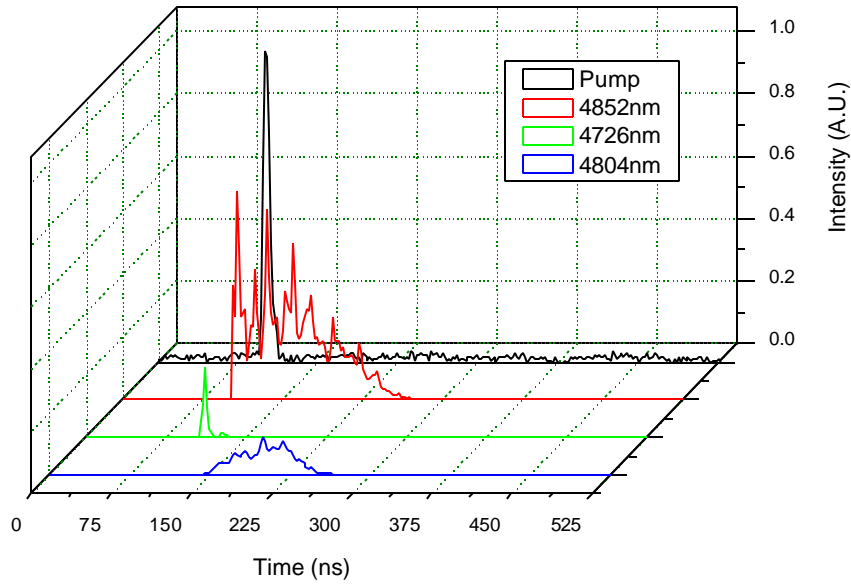


Figure 4.15. Spectrally resolved lasing output with a 70% reflective output coupler, and 20 Torr of CO.

The effect of pressure on lasing efficiency was also studied experimentally and theoretically. A comparison between the numerical model and experimental results is presented in Figure 4.17. The numerical model agrees well with the experimental data.

4.4 Discussion

Overall the experiments were a success and optically pumped cascade lasing around 4.7 μm was demonstrated on the 2nd overtone of carbon monoxide. The data agreed well with the numerical model results, Figure 4.17, and the max optical efficiency

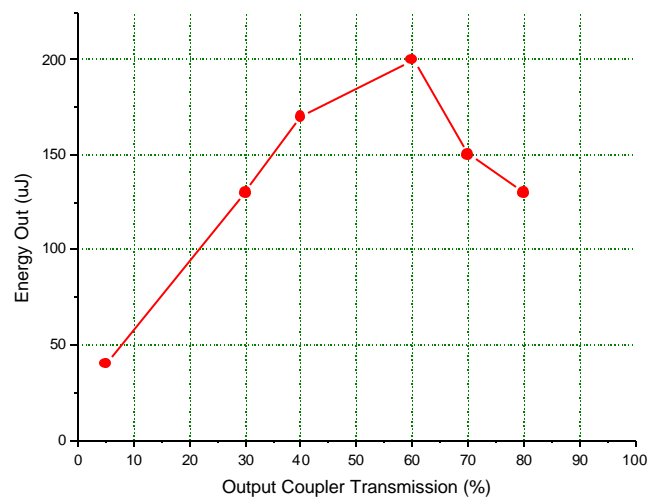


Figure 4.16. Experimental output energy versus output coupler transmission.

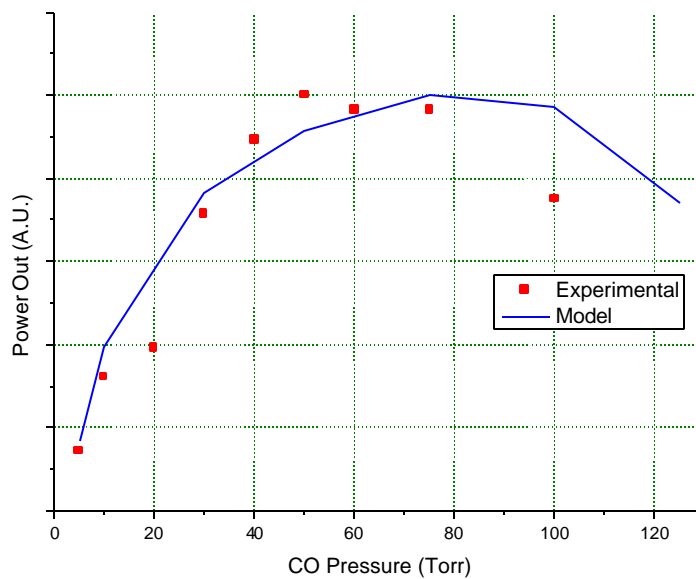


Figure 4.17. Power output versus pressure with a 40% reflective output coupler.

measured was $12 \pm 1\%$. The low optical efficiency can be partially explained by to cavity losses and older optics used in the resonator. Energy efficiency, defined as the ratio of pump energy input to the laser energy extracted from the resonator, was experimentally around $2 \pm 1\%$. The low energy efficiency can be attributed to low pump absorption (a maximum of 25% of the pump was absorbed). The numerical model suggests overall energy efficiency at room temperature using a double pass 2 m cell can approach 8 % with a high Q-cavity, with an optical efficiency of 33%. As the pump absorption approaches 100 %, both the energy efficiency and optical efficiencies improve drastically to 32%.

The model lacked the ability to accurately describe the temporal output of the CO laser since it did not incorporate the resonator modes into the calculations. However, it proved useful in determining overall lasing trends. The model also lacked an ASE term, which also accounted for some the discrepancies between predictions and measurements.

Future experimental investigation should include cooling the CO cell to 100K in order to increase the absorption efficiency. The CO should also be heated, which has known draw backs. However, the higher $v(0,3)$ rotational levels have energy gaps closer to the 1550 nm wavelength of Erbium fiber lasers. Another improvement would be to fine tune the OPO and amplify the 1567 nm pump pulse. These steps would increase the photon flux through the CO cell, and improve upon the power output. The numerical model could be improved with the addition an ASE term.

The data did not show much benefit in cascade lasing, since the highest powers measured were without cascade lasing. This leads to the question of why bother with the small absorption cross-sections of 2nd overtone pumping and the absorption problems it poses. Instead, a 2.3 μm GaSb diode laser could be used as a 1st overtone optically pumped source. The absorption cross section at 2.3 μm is over 100 times larger. The 2.3 μm diode laser is not at the same developmental stage as the Erbium fiber lasers, and lacks the high power to produce a significant 4.7 μm laser.

CHAPTER FIVE: FUTURE STUDY

The method used to create an optically pumped CO laser is inherently unscalable. Since, OPO's do not scale linearly and are non-trivial devices to package in a turn key system the pump source is currently the limiting factor on optically pump CO overtone laser's efficiency and power level. In order to increase the CO laser's output power a more powerful pump source must be explored. Currently, high power fiber lasers are developing dramatically, and have already surpassed the 1kW average power per fiber level. The idea of using fiber lasers to optically pump CO will be briefly explored.

Fiber lasers currently pose two difficulties in optically pumping CO. First, they operate at extremely high repetition rates which can be considered continuous wave, CW, operation. Second, they typically have a very large bandwidth range. The large bandwidth decreases the absorption efficiency. Research is currently underway to narrow band a high power fiber laser around the $v(0,3)$ transition wavelength, 1567nm.

CW operation is a problem since the intensity drops drastically compared to pulse operation. This behavior hints the power levels required to adequately pump the 2nd overtone of CO with fiber lasers may be unreasonably high. The numerical model described in Appendix C was used to run a numerical study on CW pumping of CO.

A long trapezoidal pulse was used to approximate a CW pump source. The pulse length was set to 2000 ns, which was long enough for the CO laser to reach steady state, as shown Figure 5.1. The model outputs the absorption efficiency and

the energy efficiency. Absorption efficiency is defined as the percentage of the pump beam absorbed, and the energy

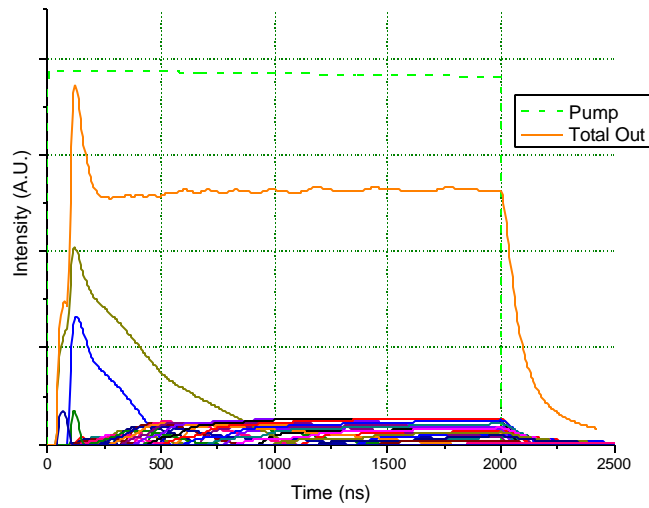


Figure 5.1. CO laser output with a 25kW CW pump source. The green trace is the scaled pump, and the orange trace is the total laser output. The blur of lines are high rotational level lasing lines due to a partial population inversion.

efficiency is the fraction of pump energy over CO energy extracted from the resonator.

Table 5.1 has a list of the model parameters used to pump the $v(0,3)$ R(2) line.

Table 5.1. Model input conditions for CW pumping runs.

MODEL PARAMETERS	
CO Pressure	30 Torr
Gain Length	100 cm
Resonator Length	110 cm
Output Coupler	90% R
Pump Diameter	0.30 cm
Pump FWHM	100 MHz
Pump Pass	50

The first parameter explored was the effect on CW pump power versus CO laser efficiency. Model runs were done at two temperatures, 298K and 100K. At lower temperatures a smaller Boltzmann distribution is obtained, see Figure 5.2. These conditions raise the efficiency by increasing the amount of the pump that can be absorbed before the pump transition is saturated, and the lower rotational states have a much larger cross section.

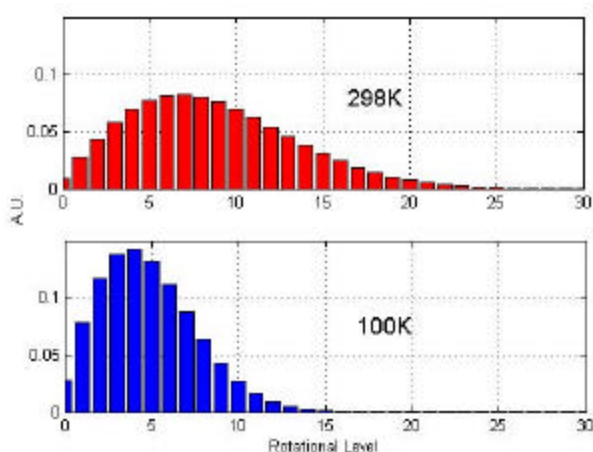


Figure 5.2. Boltzmann rotational distribution for the ground state of CO. Notice the number of molecules in $J = 4$ at 100 K is approximately double that of $J = 6$ at 298 K.

The increased absorption cross section allows a higher percentage of the pump beam to be absorbed. In other words it reduces the effective gain length needed to obtain 100% absorption. The pump beam is 97% at 298 K and 99% at 100 K absorbed in the analyses represented in Figure 5.3. The pump beam saturates the transition around 7.5 kW at 298 K. The pump does not saturate the transition at 100 K even at powers over 50 kW, as shown in Figure 5.4 and 5.5.

An intensity saturation curve, Figure 5. 6, was modeled under the conditions in Table 5.1. Results indicate that the gain is still high in the partial inversion since the model predicts lasing at very high output coupler transmissions

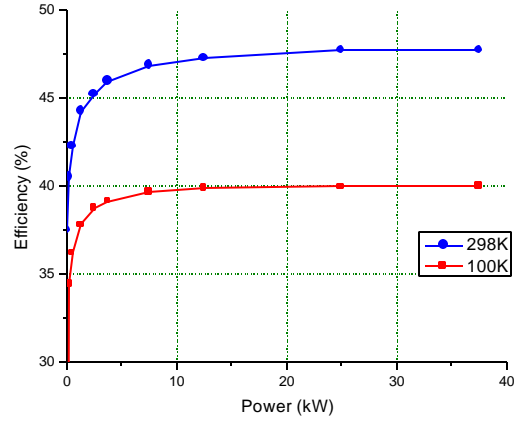


Figure 5.3. Efficiency versus pump power under the conditions listed in Table 1.

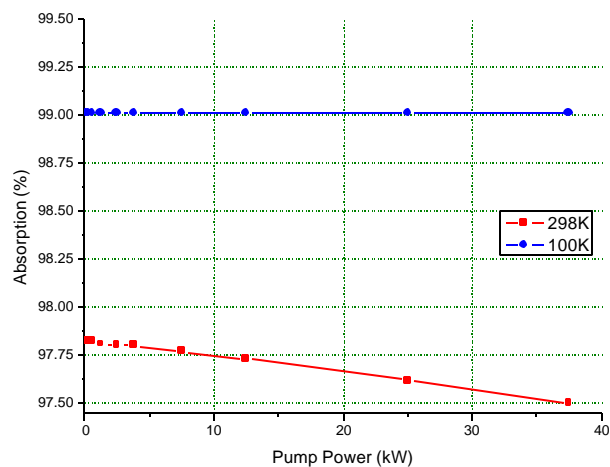


Figure 5.4. Absorption versus pump power. This shows the effect of saturation on the pump beam absorption. Running at cooler temperatures allows for more of the pump to be absorbed, thus increasing the efficiencies.

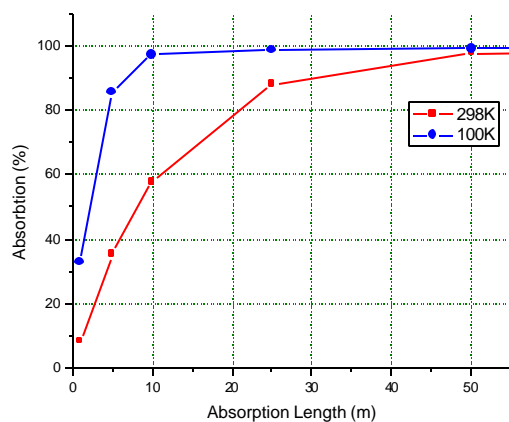


Figure 5.5. Absorption versus path length with 30 Torr of CO. At 100K 99% of the beam is absorbed within 10 meters, at 298K 50 meters is required.

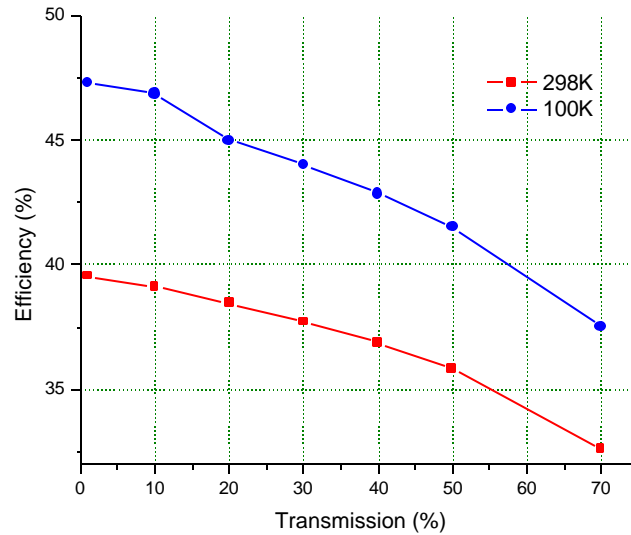


Figure 5. 6. The Isat curve for 30 Torr of CO at 298K and 100K.

The numerical results show promise in the ability to CW pump CO, with very high efficiencies. The model indicates the small absorption on the 2nd overtone can be overcome by cooling the CO to 100K reducing the length required from 50 m to 10 m for 99% pump absorption. The overall energy efficiency approaches 50% for CW powers over 12kW.

REFERENCES

1. C.K.N. Patel and R.J. Kerl, "Laser oscillation on the $X\Sigma +$ vibrational rotational transitions of CO," *Applied Physics Letters*, **5**, 1964, pp 81.
2. R.M. Osgood, Jr. and W. C. Eppers, Jr., "High Power CO-N₂-He laser," *Applied Physics Letters*, **13**, no. 12, pp. 409-411, 1968.

3. R.M. Osgood, Jr. and W. C. Eppers, Jr., "An investigation of high-power CO laser," *IEEE J. Quantum Electron.*, **QE-6**, March 1970, pp. 145-154
4. J.E. McCord, H.C. Miller, G.D. Hager, A.I. Lampson, and P.G. Crowell, "Experimental investigation of an optically pumped mid-infrared carbon monoxide laser," *IEEE J. Quantum Electron.*, **35**, 1999, pp 1602-1612.
5. J.E. McCord, A.A. Ionin, S.P. Phipps, A.I. Lampson, J.K. McIver, A.J.W. Brown, and G.D. Hager, "Frequency-tunable optically pumped carbon monoxide laser," *IEEE J. Quantum Electron.*, **36**, 2000, pp 1041-52.
6. C.S. Kletecka, N. Campbell, C.R. Jones, J.W. Nicholason, W. Rudolph, "Cascade Lasing of Molecular HBr in the Four Micron Region Pumped by a Nd:YAG laser," *IEEE J. Quantum Electron.*, **40**, 2004, pp 1471-7.
7. H.C. Miller, J.E. McCord, S.J. Davis, J. Kessler, D.B. Oakes, G.D. Hager, "Optically pumped mid-infrared hydrogen chloride laser," *J. Appl. Phys.*, **84**, 1998, pp 3467-73.
8. H.C. Miller, D.T. Radzykewyca, Jr., G.D. Hager, "An optically pumped mid-infrared HBr laser," *IEEE J. Quantum Electron.*, **30**, 1994, pp 2395-2400.
9. D.A. McQuarrie, J.D. Simon, *Physical Chemistry A Molecular Approach*, University Science Books, Sausalito CA (1997), p. 323
10. D.A. McQuarrie, p. 323.
11. D.A. McQuarrie, p. 198.
12. T. George, W. Urban, and A. Le Floch, "Improved mass-independent Dunham parameters for the ground state of CO and calibration frequencies for the fundamental band," *J. Molec. Spec.*, **165**, 1994, pp. 500-5.
13. C.F. Wisniewski, *Spatially Resolved sub-doppler overtone gain measurements in small scale supersonic HF laser*, University of New Mexico, Albuquerque NM, 2003.
14. D.A. McQuarrie, p. 501.
15. D.A. McQuarrie, p.527-35.
16. D.A. McQuarrie, p. 711.

17. Conversations with Dr. Gordon Hager at AFRL.
18. S.P. Phipps, *Rotational relaxation in carbon monoxide*, University of New Mexico, Albuquerque NM, 2001.
19. S.P. Phipps, T.C. Smith, M.C. Heaven, J.K. McIver, W.G. Rudolph, and G.D. Hager, "Investigation of the state-to-state rotational relaxation rate constants for carbon monoxide (CO) using infrared double resonance," *J. Chem. Phys.*, **116**, 2002, pp.9281-92.
20. J.T. Verdeyen, *Laser Electronics*, Prentice Hall, Upper Saddle River NJ (1995), pp. 179-82.
21. J.T. Verdeyen, pp. 183-87.
22. J. Henningsen, H. Simonsen, T. Mogelberg, and E. Trudso, "The 0-3 overtone band of CO: Precise linestrengths and broadening parameters," *J. Mol. Spectrosc.*, **193**, 1999, pp. 354-62.
23. A.E. Siegman, *Lasers*, University Science Books, Sausalito CA (1986), pp. 547-557.
24. J.T. Verdeyen, pp. 237.
25. A.E. Siegman, pp. 432-35.
26. J.T. Verdeyen, p. 133.
27. H. Weichel, and L.S. Pedrotti, "A cummary of useful laser equations –an lia report," *Elec. Opt. Sys. Des.*
28. P.W. Milonni, and J.H. Eberley, *Lasers*, John Wiley & Sons, New York NY (1988), p. 382.
29. J.T. Verdeyen, p. 151.
30. K. Okada, M. Aoyagi, and S. Iwata, "Accurate evaluation of Einstein's A and B coefficients of rovibrational transitions fro carbon monoxide: spectral simulations of $\nu=2$ rovibrational transitions in the solar atmosphere observed by a satellite," *J. Quan. Spectrosc. Rad. Trns.*, **72**, 2002, pp. 813-25.
31. J.M. Hure and E. Reueff, "Analytic representations of rovibrational dipole matrix elements for the CO molecule," *Astron. Astrophys. Suppl. Ser.*, **117**, 1996, pp. 561-68

32. B.R. Rafferty, et. al., "Experimental and theoretical investigation of coaxial pumped photolytic atomic bromine laser," *IEEE J. Quantum Electron.*, **33**, 1997, pp. 685-704.

APPENDIX A: DATA PLOTS

This appendix contains all of the data collected for the long gain and resonator setup. The specifications listed in Table A.1 are valid for all plots in appendix A.

Table A. 1. Specifications for all data presented in Appendix A.

CO Laser Specifications	
Gain Length	182 cm
Resonator Length	233 cm
Cavity Round Trip	15.5ns
Cavity FSR	64.4MHz
MaxR	98% R
Radius of Curvature	500 cm
Pump Transition	v(0,3)R(6)
Pump Wavelength	1568.77nm

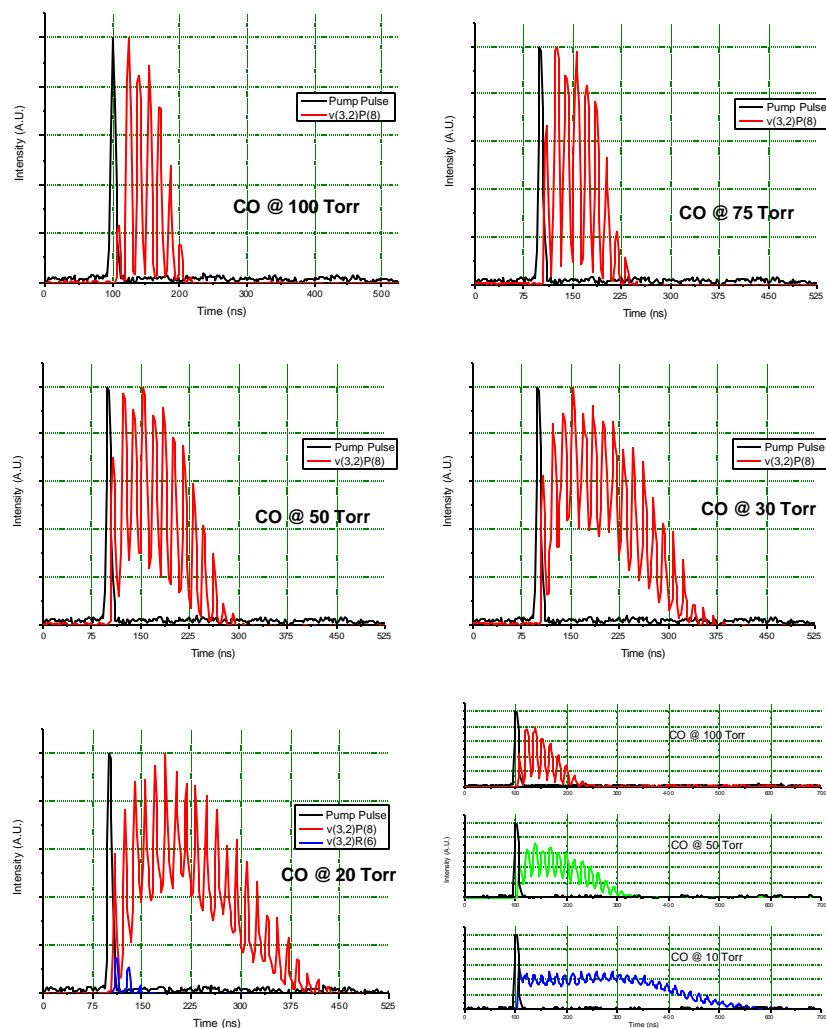


Figure A.1. 95% reflective output coupler and 100 - 10 Torr of CO.

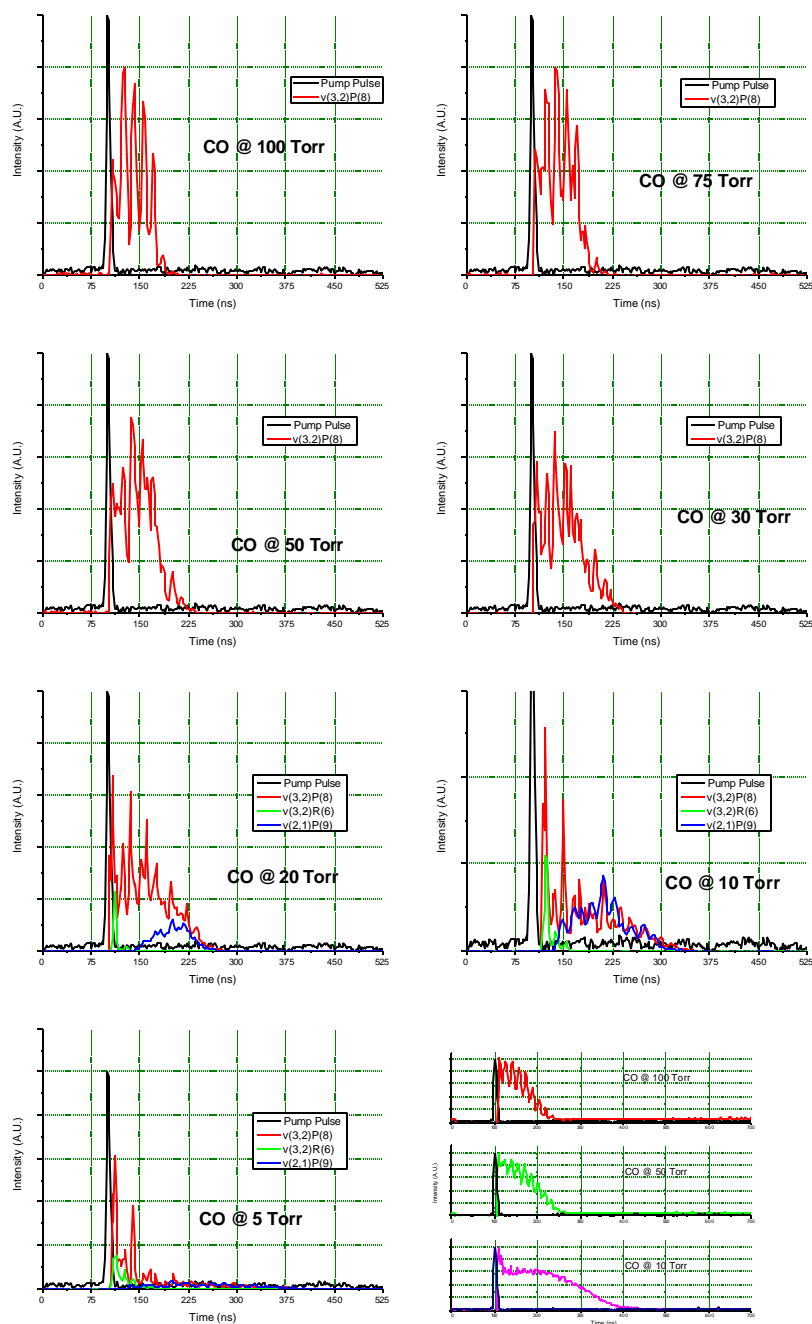


Figure A.2. 70% reflective output coupler and 100 - 5 Torr of CO.

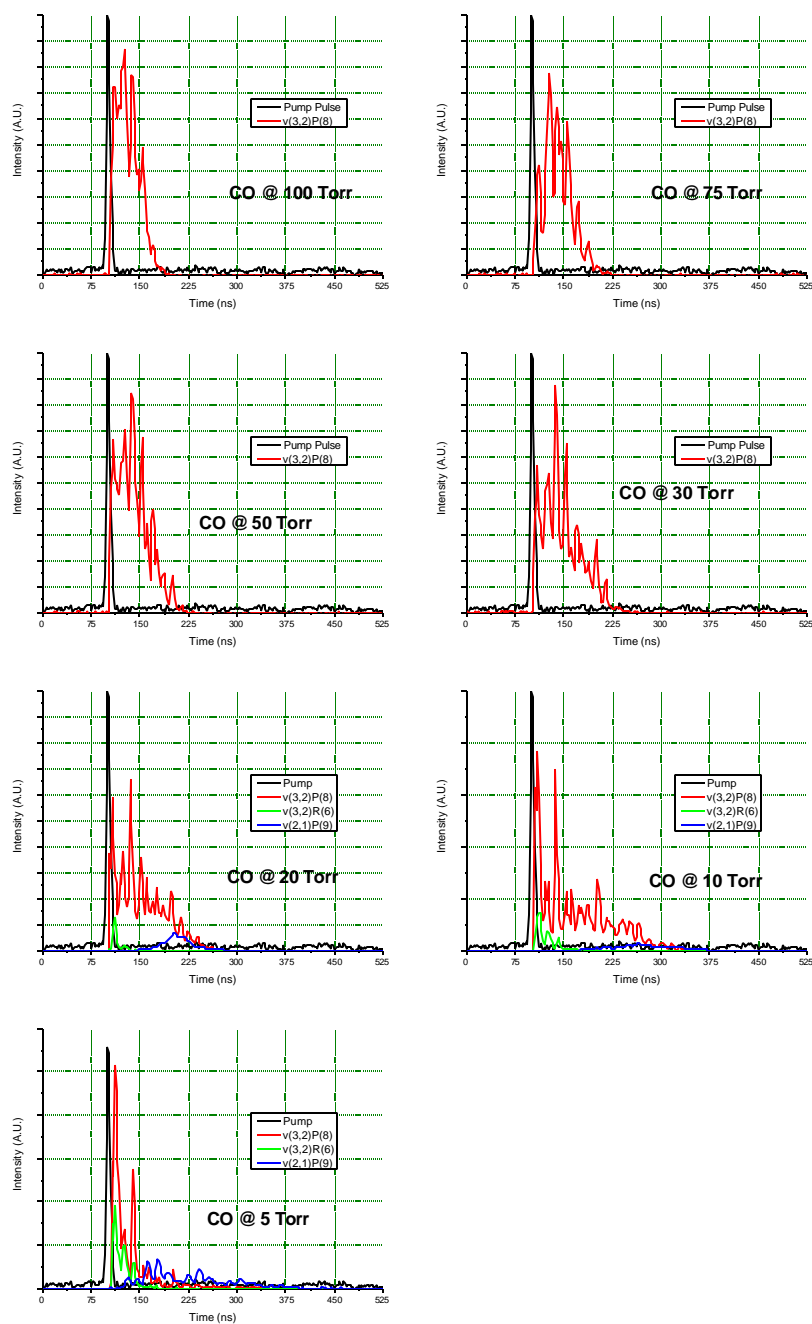


Figure A.3. 60% reflective output coupler and 100 - 5 Torr of CO.

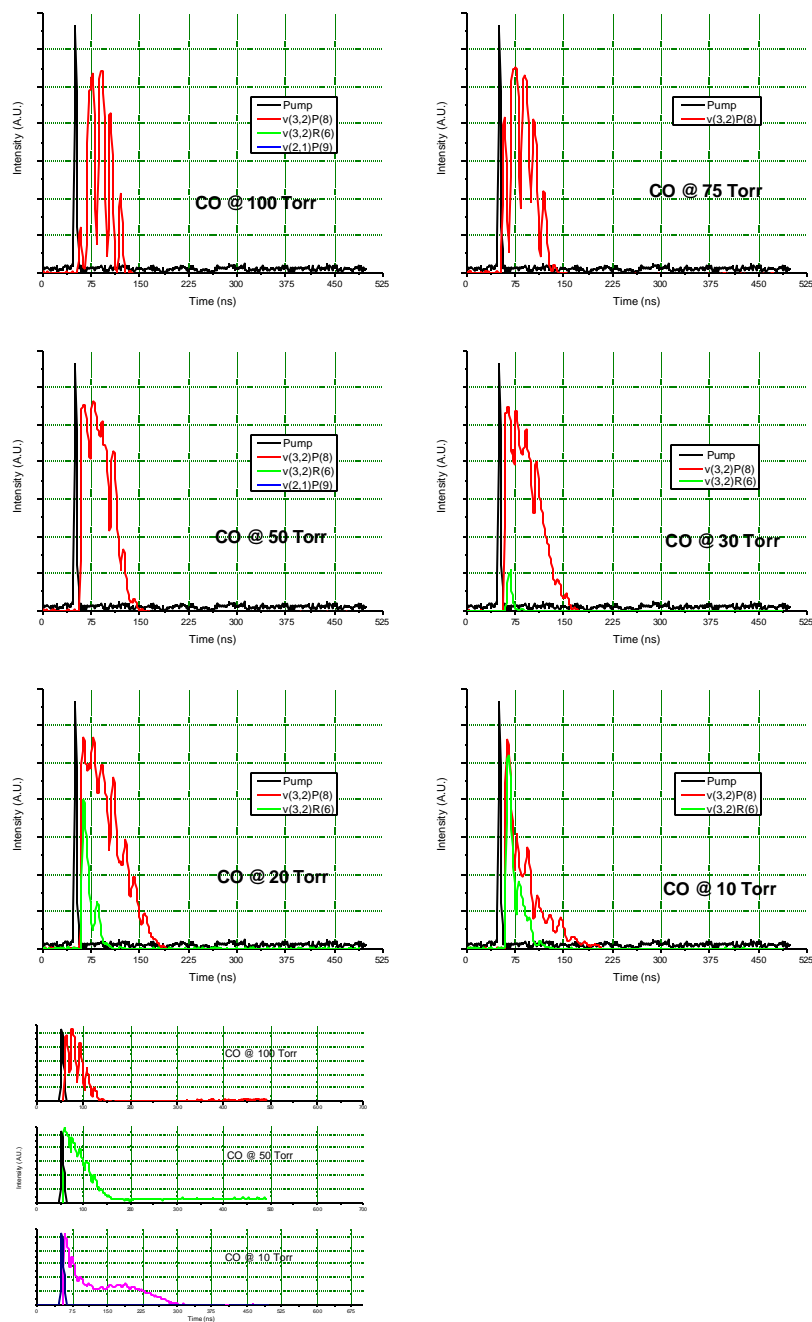


Figure A.4. 40% reflective output coupler and 100 - 5 Torr of CO.

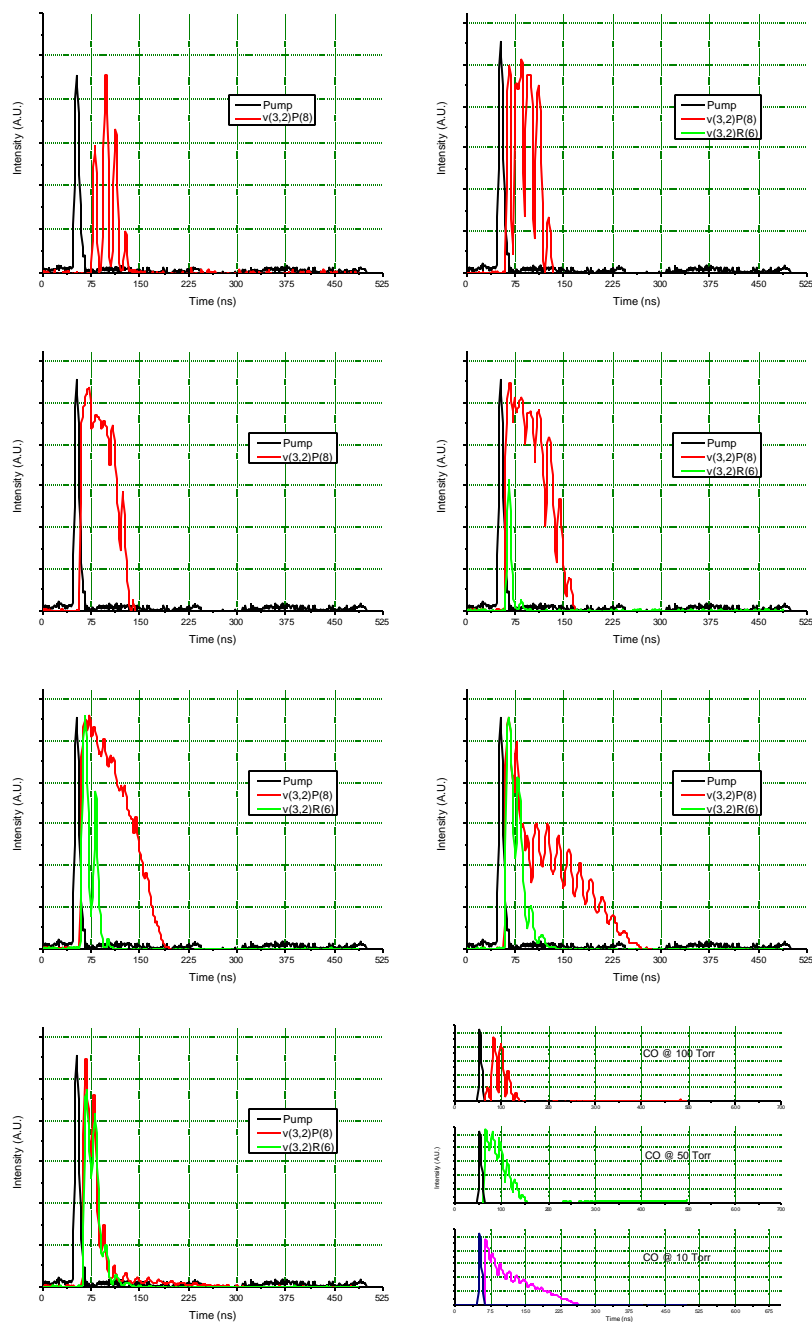


Figure A.5. % reflective output coupler and 100 - 5 Torr of CO.

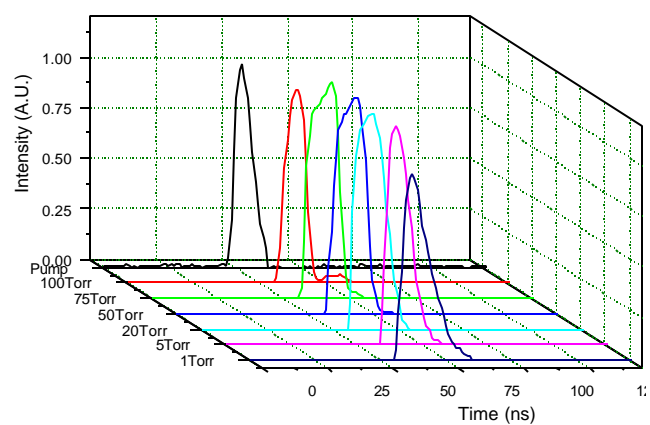
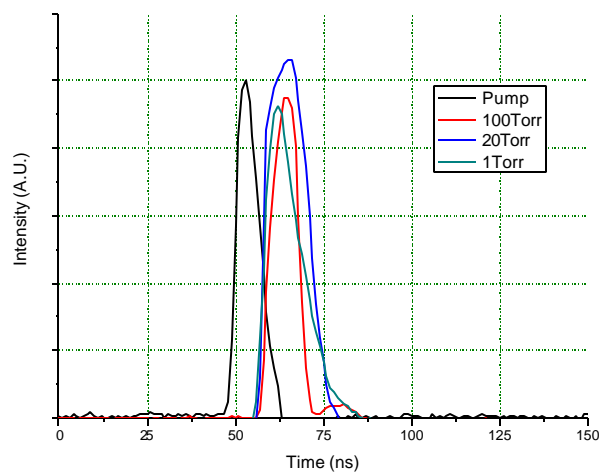


Figure A. 6. ASE emission plots for various pressures.

APPENDIX B: LINEWIDTH EXPERIMENTS

Linewidth experiments used the OPO's diode seed laser as a tunable probe over the $v(0,3)$ transition. The scanning laser output was controlled and data collected using a computer employing LabVIEW software and National Instruments DAQ hardware. The computer controlled the output wavelengths, scan range, and the scan rate. The central output wavelength was set by coarsely tuning an intracavity diffraction grating of the diode, and the fast tight scans were accomplished by a piezo electric motor that fine tuned the wavelength out. The piezo was driven by a voltage ramp generated by the LabVIEW control software. The scan rate was adjusted by recycling the voltage rise across the diode at rates of up to 50 Hz. Resolution on the frequency control was 500 samples per scan.

The diode laser beam was split two ways. The input measurements where data collected on a reference cell was used to determine if the correct wavelength range was being scanned, and Fabry-Perot Interferometer to correctly calibrate the x-axis to units of frequency.

A Fabry-Perot Interferometer was used to correctly calibrate the x-axis to one of frequency versus samples. Data was read into the system based only on a per sample calibration. For the results of the absorption measurements to have any meaning, the x-axis must be calibrated to that of frequency. In order to do so, it was necessary to read the output of the laser diode on a Fabry-Perot Interferometer. Since the scan range was approximately 2.4 GHz, a 300 MHz Fabry-Perot Interferometer was used to

ensure enough peaks could be measured for adequate calibration. Using the known value of 300MHz for a full spectral range peak and comparing that value to the number of samples between peaks, a valid value of frequency could be measured on the data acquisition readout.

LabVIEW software then collected the absorption with an accurate frequency axis, and saved the data to a text file. This data was then fit to a Voigt function using Origin's software package. In order to get accurate Gaussian and Lorentzian widths the relationships temperature and pressure must be maintained. The Gaussian linewidth is related only to the temperature of the gas by

$$w_G = 2 \ln(2) \nu_0 \sqrt{\frac{T}{M}} \quad (\text{B-1})$$

where w_G is the Gaussian (Doppler) width, ν_0 is the line center frequency, T is the temperature, and M is the reduced mass. The Lorentzian width is related to both the temperature and pressure of the gas by

$$w_L = \frac{296}{T} \sum_i 2g_i P_i \quad (\text{B-2})$$

where w_L is the Lorentzian width, g is the pressure broadening coefficient [MHz/Torr] of species i, and P is the pressure of the species i. When fitting with a Voigt function the resulting Gaussian and Lorentzian width must be consistent [1]. This simply means the temperature corresponding to both widths must agree.

Using the above procedure to fit absorption curves at various pressures of CO the pressure broadening coefficient can be experimentally measured.

REFERENCES

1. G. C. Manke, "Procedures for extracting temperature and concentration from measure spectral lineshapes," Air Force Research Laboratory, 2003.

APPENDIX C: Numerical Model Description

The rate equation model was developed using existing code to model the optically pumped CO laser. The model included terms for rotation relaxation, vibrational-vibrational, vibrational-rotational, and radiative processes. The model did not originally contain any spatial dependence, longitudinal or radial, and simply assumed the entire gain region changed only in time. The model employed a robust ordinary differential equation solver to solve the 120 coupled differential equations. This section heavily references the model developed by Rafferty et. al [1].

The rate equations used can be written as one equation with rate constants for each individual rovibrational level. This results in 120 (30 rotational levels and 4 vibrational levels) coupled differential equations. Rate equations are based on of Chapter 2 theoretical discussion of the radiative processes and their effects on the population inversions.

The model will be developed here under two processes, radiative and non-radiative. Radiative processes include spontaneous and stimulated emission, and the non-radiative processes include the above mentioned kinetics. The time rate of change of the number of photons in the cavity is dependent upon the gain and is given by

$$\frac{dN_p}{dt} = \frac{cL_g}{d}(\mathbf{a} - \mathbf{a}_{th})N_p \quad (\text{C-1})$$

where N_p is the number of photons, \mathbf{a} is the gain between the upper and lower levels, \mathbf{a}_{th} is the threshold gain, d is the resonator length, and L_g is the gain length. It is important to notice that if $N_p = 0$ at $t = 0$, then for all times $N_p = 0$. This shortcoming is corrected by adding a spontaneous emission, noise, term to equation 1. However, it is simpler to deal with circulating intensities within the cavity rather than photon numbers. The two way average intensity is related to the number of photons by

$$I = c \left(\frac{N_p}{V} \right) h\nu \quad (\text{C-2})$$

where V is the mode volume. Rewriting equation 1 in terms of intensity and adding the spontaneous emission term results in

$$\frac{dI}{dt} = \frac{cL_g}{d}(\mathbf{g}(v, J) - \mathbf{g}_{th})I + \frac{c^2 h\nu [N_U]}{V} \mathbf{s} \quad (\text{C-3})$$

where the last term is the spontaneous emission. Gain is a function of the population inversion and was given as equation 2.57, and is repeated here in terms of the CO rovibrational inversions for both P and R branch lasing transitions.

$$\mathbf{g}(v, J) = \mathbf{s}_{P,R}(v, J) \left[N(v, J) - \frac{(2J+1)}{(2(J\pm 1)+1)} N(v-1, J\pm 1) \right] \quad (\text{C-4})$$

This approach implies that the rate equations for the population inversions must be developed in order to calculate the circulating intensity in equation 3.

Assuming no longitudinal dependence, the energy is absorbed uniformly in the pumped volume which leads to the following source terms for the 2nd overtone population [32].

$$[N_U] = \frac{E_{abs}}{h\nu} \cdot \frac{1}{V} \quad (C-5)$$

Where E_{abs} is the absorbed energy of the pump beam, and V is the mode volume. The time dependent source terms assuming a Gaussian pump pulse is described by

$$W_{Upper}(t) = [N_U]_0 \frac{2}{t_p} \sqrt{\frac{\ln(2)}{p}} \exp\left(-4 \ln(2) \left(\frac{t-t_0}{t_p}\right)^2\right) \quad (C-6)$$

$$W_{Lower}(t) = [N_L] - [N_U]_0 \frac{2}{t_p} \sqrt{\frac{\ln(2)}{p}} \exp\left(-4 \ln(2) \left(\frac{t-t_0}{t_p}\right)^2\right) \quad (C-7)$$

where t_p is the pump pulse's temporal width, and t_0 is the location of the peak in time.

Equation 6 is the only source term for the 2nd overtone manifold. Each rotational level will have its own rate equation describing the population as a function of time. Each rate equation will include RR, VV, VT, stimulated emission, and spontaneous emission source and sink terms for all allowed transitions. Only RR will be included in the model since VV and VT take place on time scales much larger than the lasing. Only the specific rovibrational pumped will have pumped source terms, which drives the remainder of the system. The generic rate equation for the pumped level and non-pumped level are given by:

$$\frac{dN(v,J)}{dt} = W_{upper}(t) - g_p(v,J) - g_R(v,J) - A[N(v,J)] + B(v,J) \quad (C-8)$$

$$\frac{dN(v, J)}{dt} = g_p(v+1, J-1) + g_R(v+1, J+1) - g_p(v, J) - g_R(v, J) - A[N(v, J)] + B(v, J) \quad (C-9)$$

$$\frac{dN(v, J)}{dt} \Big|_{Ground} = g_p(v+1, J-1) + g_R(v+1, J+1) + B(v, J) - W_{Lower}(t) \quad (C-10)$$

where the $B(v, J)$ terms represent rotational relaxation into and out of a rotational level, and $A[N(v, J)]$ represents spontaneous emission. Equation 8 is the rate equation for the specifically pump rovibrational level, equation 9 is for all other rovibrational levels, and equation 10 is represents the rovibrational level pumped from.

The model was run under a variety of conditions such as: including all kinetics or only a select few kinetic terms. It was observed that the numerical model produced similar results with and without VV and VT kinetics included. Thus, the model was typically run without VV and VT to decrease the computation time. Figure C.1 has an example of data collected with various effects excluded.

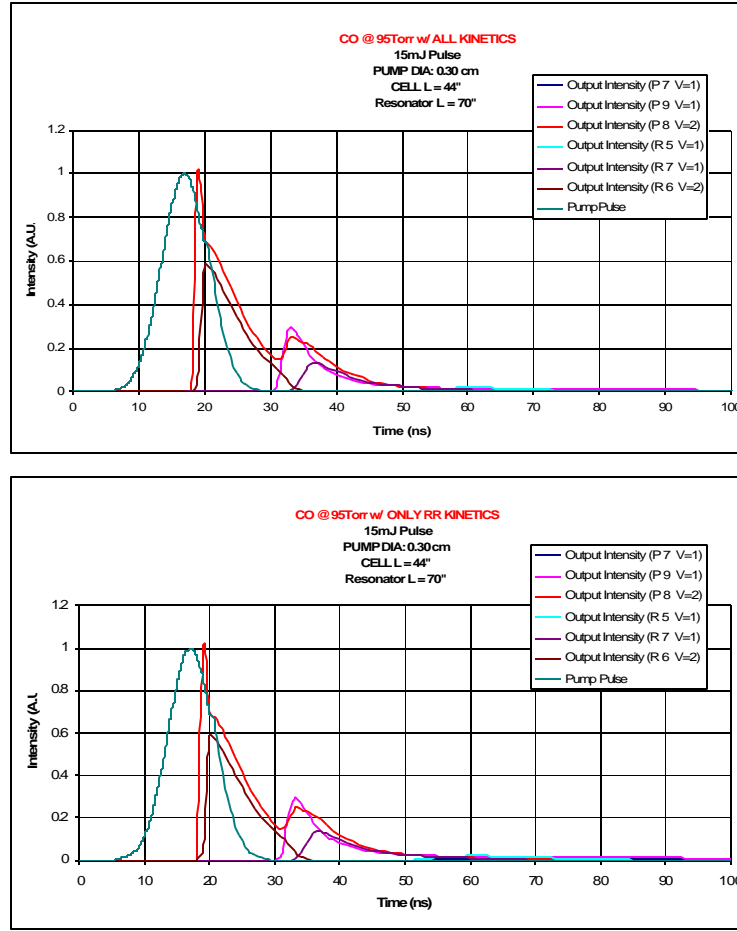


Figure C. 1. The negligible effects of VV and VT kinetics.

The model lacked a few pertinent parameters such as a longitudinal and radial spatial dependence. The gain was considered spatially uniform in the model which was not the case experimentally. The model also lacked an ASE or super radiance term which was a dominant factor in the experimental data. The final improvement would be to include a model of the radiation in the cavity so the transverse and axial modes

could be accounted for, and mode locking effects could be modeled. A typical model output plot is in Figure 1. It does not show any of the typical temporal variations of the experimentally collected data, since mode beating effects are not included in the model.

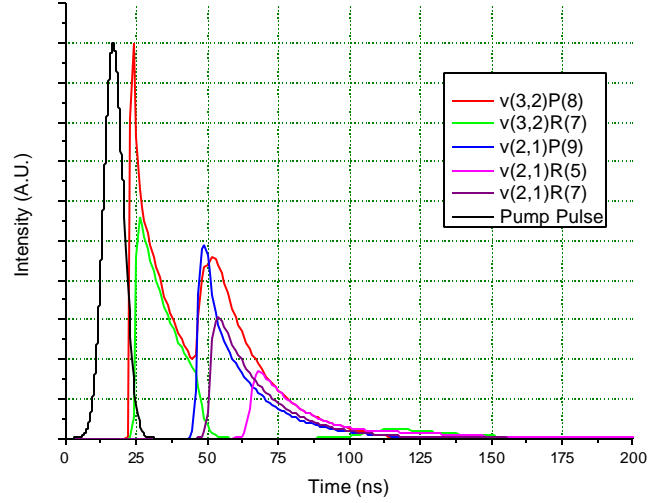


Figure C.2. Model output of an $v(0,3)R(6)$ pump case closely matching experimental run conditions.

The model does not accurately predict the temporal output of the CO laser due to the missing attributes mentioned above. However, the model reasonably predicts overall trends in the CO laser efficiency versus pressure, output coupler reflectivity, and path length effects.

REFERENCES

1. B.R. Rafferty, et. al., "Experimental and theoretical investigation of coaxial pumped photolytic atomic bromine laser," *IEEE J. Quantum Elctron.*, **33**, 1997, pp. 685-704.

DISTRIBUTION LIST

DTIC/OCP 8725 John J. Kingman Rd, Suite 0944 Ft Belvoir, VA 22060-6218	2 cys
AFRL/VSIL Kirtland AFB, NM 87117-5776	2 cys
AFRL/VSIH Kirtland AFB, NM 87117-5776	1 cy
Official Record Copy AFRL/DELC/David A. Hostutler	1 cy
Kip Kendrick AFRL/DELC	1 cy

